Intrinsic and extrinsic inhibition of cortical flow underlies symmetry breaking during unilateral cytokinesis

-Author names and Affiliations

Christina Rou Hsu[1,2], Gaganpreet Sangha[1,2], Wayne Fan[1,2], Joey Zheng[1,2], and Kenji Sugioka[1,2*]

[1]Life Sciences Institute, The University of British Columbia, 2350 Health Sciences Mall, Vancouver, BC V6T1Z3, Canada

[2]Department of Zoology, The University of British Columbia, 2350 Health Sciences Mall, Vancouver, BC V6T1Z3, Canada

***Corresponding author**

Kenji Sugioka

Life Sciences Institute, Department of Zoology, The University of British Columbia, 2350 Health Sciences Mall, Vancouver, BC V6T1Z3, Canada

sugioka@zoology.ubc.ca

Phone: +1-604-404-3150

Short title

Symmetry breaking in unilateral cytokinesis

Summary

Non-concentric closure of the contractile ring, known as unilateral cytokinesis, often orients along the body axis to maintain tissue integrity in various animals. Despite the identification of unilateral cytokinesis regulators, the mechanism of initial symmetry breaking remains elusive. Here, we report that intrinsic and extrinsic inhibition of cortical flow breaks cytokinesis symmetry in *Caenorhabditis elegans*. By coupling high-resolution 4D imaging with an *in vitro* cell contact reconstitution assay, we found that unilateral cytokinesis of the zygote P_0 and the two-cell stage blastomere AB are regulated by actin-dependent and adhesion-dependent mechanisms, respectively. Intracellular compression and intercellular adhesion in P_0 and AB, respectively, locally inhibit both furrow-directed cortical flow and cleavage furrow ingression, resulting in eccentric ring closure. Our study demonstrates that local mechanical suppression of ring-dependent cell cortex pulling is a common symmetry-breaking cue underlying distinct modes of unilateral cytokinesis.

Keywords: Cytokinesis, cortical flow, C. elegans, Contractile ring, Coronin, Anillin, Actin, Myosin, Cell division

Introduction

The contractile ring is a supramolecular structure critical for the physical partitioning of dividing cells, but its function is not limited to cell proliferation. In animal zygotes and epithelial tissues, contractile ring closure is often non-concentric and is termed unilateral or asymmetric cytokinesis (Rappaport, 1996; Sugioka, 2021; Thieleke-Matos et al., 2017). This phenomenon is ubiquitously observed from invertebrates to vertebrates, including humans (Ferguson, 1988; Jinguji and Ishikawa, 1992; Maddox et al., 2007; Vogetseder et al., 2005; Ziegler, 1903), and its disruption is associated with cytokinesis failure and epithelial sheet and tube morphogenesis defects (Herszterg et al., 2013; Maddox et al., 2007; Taulet et al., 2017). Despite its developmental significance, the mechanism of unilateral cytokinesis remains unclear on several points.

A classically-known symmetry-breaking cue of unilateral cytokinesis is mitotic spindle positioning, which is critical for specifying contractile ring assembly at the equator of the cell cortex (Rappaport, 1986; Rappaport and Conrad, 1963). Central to contractile ring formation is the activation of the small GTPase RhoA (Figure 2A) (Basant and Glotzer, 2018). Upon anaphase onset, the chromosome passenger complex recruits centralspindlin to the spindle midzone and activates its oligomerization (Basant et al., 2015; Douglas et al., 2010). Centralspindlin then activates Ect2 RhoGEF, which in turn facilitates the formation of the active GTP-bound form of RhoA at the equatorial cell cortex (Gómez-Cavazos et al., 2020; Somers and Saint, 2003; Tatsumoto et al., 1999; Yüce et al., 2005). RhoA then stimulates downstream Rho-kinase and the actin nucleating/polymerizing factor formin to promote myosin II activation and F-actin assembly, respectively, to initiate the ring formation (Matsumura, 2005; Otomo et al.,

2005). Pioneering studies have shown that the asymmetric positioning of the mitotic spindle, with the spindle midzone closer to one side of the equatorial cortex, is sufficient to induce unilateral cleavage in ctenophore zygotes and normally symmetrically dividing sea urchin embryos (Rappaport and Conrad, 1963; Yatsu, 1912). The off-center spindle induces asymmetric activation of RhoA in the adjacent cell cortex (Bement et al., 2005). Thus, the geometric relationship between the equatorial cortex and mitotic spindle is a symmetry-breaking cue of unilateral cytokinesis in some animals, hereafter called spindle-dependent unilateral cytokinesis. However, spindle-cortex proximity does not explain unilateral cytokinesis in many tissues as described below.

Epithelial cells undergo adherens junction-dependent unilateral cytokinesis. In both invertebrate and vertebrate epithelial cells, mitotic spindle is slightly nearer to the apical cell cortex, but the furrow is usually formed from the basal side (Fleming et al., 2007; Morais-de-Sá and Sunkel, 2013; Nakajima et al., 2019; Woolner and Papalopulu, 2012). Inhibition of contractile ring components such as anillin and septin does not affect ring eccentricity, but knockdown of adherens junction components results in concentric contractile ring closure in *Drosophila* embryonic and follicular epithelia (Guillot and Lecuit, 2013; Morais-de-Sá and Sunkel, 2013). Although it has been reported that the mechanical resistance imposed by adherens junctions anchors the contractile ring at the apical cortex (Guillot and Lecuit, 2013), the relationship between junctions, cell-cortex dynamics, and furrow ingression remains elusive.

In contrast with the systems described above, *Caenorhabditis elegans* zygotes undergo adhesion-independent unilateral cytokinesis. Mitotic spindle positioning is not particularly off-center, while cortical components, including myosin, anillin, and septin,

are enriched in the fast-closing furrow, forming a structurally asymmetric ring (Maddox et al., 2007). Unlike in *Drosophila* epithelial cells, anillin and septin are required for structural asymmetry and unilateral cleavage (Maddox et al., 2007). Recent studies have also revealed the significance of the concerted movement of cell-cortex material, or cortical flow, during this process (Figure 2A). Furrow-directed cortical flow compresses the cell cortex along the axis perpendicular to the contractile ring and facilitates myosin enrichment and F-actin alignment along the circumferential axis of the contractile ring (Khaliullin et al., 2018; Reymann et al., 2016). Formin also reinforces F-actin alignment through a filament-guided filament assembly mechanism (Li and Munro, 2021). Importantly, ring constriction further pulls the cell cortex toward the equator, producing a positive-feedback loop between cortical flow and ring constriction (Khaliullin et al., 2018). Because asymmetric myosin enrichment, eccentric closure, and asymmetric cell cortex compression have been reported to occur simultaneously (Khaliullin et al., 2018; Maddox et al., 2007), the initial symmetry-breaking mechanism remains unknown.

In this study, we performed a comparative analysis of adhesion-dependent and adhesion-independent unilateral cytokinesis using *C. elegans* as a model system, to gain insights into a unified mechanism underlying these seemingly very distinct division modes. Although implicated in the previous studies, there was no concrete evidence supporting adhesion-dependent unilateral cytokinesis in *C. elegans* (Bourdages et al., 2014; Koyama et al., 2012). We found that the two-cell stage AB cell underwent adhesion-dependent unilateral cytokinesis. Using blastomere isolation assays, high-resolution 4D imaging, and *in vitro* cell-contact reconstitution assays, we have identified symmetry-breaking cues underlying both modes of unilateral cytokinesis.

Results

High-resolution 4D imaging and quantitative analysis of contractile ring dynamics

To understand the symmetry-breaking mechanism of unilateral cytokinesis, we performed high-resolution 4D imaging of GFP-fused non-muscle myosin II (NMY-2) (Figure 1A, Figure S1A). Imaging methods widely adopted in the *C. elegans* cytokinesis field slightly compress embryos to facilitate visualization of the cell cortex (Khaliullin et al., 2018; Li and Munro, 2021; Reymann et al., 2016). However, these methods are not optimal to analyze early symmetry-breaking events, because compression is known to induce global cortical rotation along the short axis of the cell (Schonegg et al., 2014; Singh et al., 2019) (Figure S1B). The compression-induced cortical rotation alters the positioning of fast- and slow-closing (leading and lagging, respectively) cortical sides between pre- and mid-cytokinesis, preventing the analysis of initial symmetry breaking. To avoid compression, we used cell-sized polystyrene beads as spacers between the coverslip and slide. Furthermore, we used a refractive index-matching medium and a silicone-immersion objective to reduce spherical aberration to increase spatial and temporal resolutions (Xiong and Sugioka, 2020) (Figure S1A).

These improvements enabled us to capture complete uncompressed embryonic volumes every 5.6 sec at a 1-µm step size (a total of 31 Z slices) (Figure 1A, Movie S1). To our knowledge, this is the first example of near-synchronous 4D imaging of both cortical and ring dynamics, at a sufficient time-resolution with which one can estimate the cortex movements. As expected, we did not observe cortical rotation owing to the lack of compression (Figure S1B, Movie S1). We developed an image analysis pipeline that efficiently measured the centroid and radius of the contractile ring at a given time

from thousands of raw images (Figure. 1B, Figure S1A, S1C). From these data, we calculated ring closure indices (0–100%, 100% represents complete closure) and ring eccentricities (off-center tendency). Using an initial ring radii R_0 and at a given time Rt, the ring closure index *f(t)* was defined as:

$$f\ (t) = (R_0 - R_t)/R_0 \qquad (1)$$

We defined ring eccentricity *g(t)* using Q_t, the distance between the centroids of the initial ring (C_0) and the ring at time t (C_t), as:

$$g(t) = Q_t/R_0 \quad (Q_t \leq R_0 - R_t) \quad (2)$$

The upper limit of the eccentricity at a given time point *s(t)* was limited by Rt, as:

$$s(t) = \frac{R_0 - R_t}{R_0} = f(t) \qquad (3)$$

Because *s(t)* is equal to *f(t)*, eccentricity cannot exceed the ring closure index at any time (Figure 1C and Movie S1). After analyzing multiple embryos, individual ring constriction curves versus time were aligned relative to the time at which the ring closure first exceeded 2% (Figure S1D); this allows us to detect differences in sub-percentage ring closure indices around cytokinesis onset. We defined cytokinesis onset as the 17 sec before 2% ring closure, based on the extrapolation of a line passing two data points before the 2% ring closure to 0 (Figure S1D). Our data alignment method was set to understand early symmetry-breaking events, and our data include 50–80 sec preceding cytokinesis onset, which was not reported before. Thus, our method allows analysis of early cortical dynamics of the uncompressed embryo at high temporal resolution while preserving the initial positioning of both leading and lagging cortices, which is necessary to understand the symmetry-breaking mechanism.

Intrinsic and extrinsic control of unilateral cytokinesis in P_0 and AB blastomeres

We found that the P_0 contractile ring initially underwent nearly the upper limit of eccentric closure (Figure. 1C, $f(t) = g(t)$; Movie S1). The observed maximum ring eccentricity represents dominant furrow ingression from the leading cortex. Unilateral furrow ingression continued until approximately 89 sec after the cytokinesis onset (Figure. 1B, C; left panel). After this time point, the lagging cortex gradually started ingression, reducing eccentricity (Figure 1C, $f(t) > g(t)$; Movie S1).

Next, to compare the difference between adhesion-dependent and -independent unilateral cytokinesis, we sought an adhesion-mediated unilateral cytokinesis in *C. elegans* embryo. We focused on the two-cell stage AB blastomere that undergoes unilateral cytokinesis (Figure 1A) (Ozugergin et al., 2022). In intact embryos, the AB contractile ring initially exhibited low eccentricity, resulting in more symmetric ring closure (Figure. 1B, C; middle panel). However, as the ring constricted, eccentricity gradually increased. The distinct contractile ring dynamics in P_0 and AB indicated a qualitative difference in the unilateral cytokinesis mechanisms. To test the requirement for adhesion in AB unilateral cytokinesis, we isolated the AB cell by mechanically separating it from the neighboring P_1 cell. Obtained isolated AB cells exhibited symmetric ring closure, suggesting that AB unilateral cytokinesis is adhesion-dependent, as in *Drosophila* epithelial cells (Guillot and Lecuit, 2013; Morais-de-Sá and Sunkel, 2013).

Lack of asymmetries in mitotic spindle positioning, RhoA activity, and myosin level at the beginning of P_0 and AB cytokinesis

To address symmetry-breaking mechanisms in P_0 and AB cells, we first tested the asymmetric regulations of known contractile ring assembly pathways (Figure. 2A). First, we tested asymmetry in mitotic spindle positioning, a known symmetry-breaking cue in ctenophore zygotes (Rappaport and Conrad, 1963; Yatsu, 1912). A previous study reported symmetric spindle positioning in P_0 (Maddox et al., 2007). To analyze both P_0 and AB cells, we measured distances between centrosomes and leading (LE) and lagging cortices (LG), calculating ratios of LE to LG (Figures 2B, 2C, and S2A). In both P_0 and AB cells, the LE/LG ratio was close to 1.0, indicating mitotic spindle position symmetry relative to leading and lagging cortices. These results confirm that the geometric relationship between the mitotic spindle and cell cortex is not a symmetry-breaking cue in these cell types.

Next, we examined asymmetries of RhoA activity and myosin enrichment. To monitor the former, we used a RhoA biosensor with a GFP fused to the C-terminus of anillin containing conserved region (AH) and pleckstrin homology (PH) domains (Tse et al., 2012). Ratios between leading and lagging cortices were quantified as shown in Figure S2B. Both kymographs of the equatorial cortex and leading/lagging ratios (Figure 2D and E) show that both myosin enrichment and RhoA activity started to become asymmetric after at least 50 sec from the onset of cytokinesis. Since both were symmetric at the beginning of P_0 and AB cytokinesis, asymmetric myosin enrichment and RhoA activity do not appear to cause early symmetry breaking.

Actin alignment asymmetry specifies ring closure direction in P_0 cells

To test for actin alignment asymmetry in P_0 cells, we imaged whole Lifeact::mKate2-expressing embryos as described above (Figure 3A). For the analysis of actin filament orientation, we selected embryos that underwent furrow ingression perpendicular to the imaging plane, to have either a leading or lagging cortex at the surface of the image stack. For each embryo, ten surface slices closest to the objective lens were flattened by summation; only a central 9 × 9-µm region was analyzed to avoid deformation of the filament structure at the high-curvature surface (white dotted box in Figure 3A). Actin filament orientations were estimated based on the gradient structure tensor in a local area, using a method described before (Figure 3B, yellow lines) (Püspöki et al., 2016). We defined the circumferential axis of the ring and axis perpendicular to it as ring-axis and perpendicular-axis, respectively (Figure 2A, schematic ii). We found that the circular means of actin filament orientation at the lagging cortex were significantly higher than those at the leading cortex, indicating more ring-axis actin alignment at the lagging side (Figure 3C; $p = 0.036$ at -50 sec using Welch's t-test). The asymmetry was first observed approximately 55 sec before cytokinesis onset. As reported previously, actin orientation in both leading and lagging cortices were increasingly aligned along the ring-axis over time (Figure 3C), presumably due to the perpendicular-axis cortical compression and filament-guided filament assembly (Figure 2A) (Li and Munro, 2021; Reymann et al., 2016). In contrast, the actin signal intensities were not asymmetric at the beginning of cytokinesis (Figure 3D). These results suggest that actin alignment asymmetry specifies leading and lagging cell cortices in P_0 cells.

To examine a requirement for actin regulations in unilateral cytokinesis, we inhibited actin and actin binding proteins. A pioneering study has shown that ANI-

1/anillin is essential for unilateral cytokinesis (Maddox et al., 2007). We confirmed that *ani-1(RNAi)* caused concentric ring closure (Figure 3E-G; ring closure and eccentricity curves separate in early cytokinesis as shown in 3F). However, as anillin is a scaffold protein that interacts with F-actin, myosin II, RhoA, phosphatidylinositol, and microtubules (Liu et al., 2012; van Oostende Triplet et al., 2014; Piekny and Glotzer, 2008), the significance of anillin-dependent F-actin regulation in unilateral cytokinesis is unclear. Partial knockdown of the actin nucleator and polymerizing factor CYK-1/formin has also been reported to result in symmetric cytokinesis at the end of contractile ring closure, based on 2D analyses of compressed embryos (Chan et al., 2019), but we did not observe early unilateral cytokinesis defects in our 4D analysis of uncompressed embryos (Figure 3G).

To further investigate a requirement for actin organization in unilateral cytokinesis, we inhibited or knocked down additional actin regulators. The Arp2/3 complex mediates actin nucleation from existing filaments, leading to branched network assembly (Goley and Welch, 2006). POD-1/coronin is a negative regulator of Arp2/3 that promotes actin debranching by removing Arp2/3 from F-actin (Xie et al., 2021). Finally, we used a semi-dominant negative, temperature-sensitive mutant of one of *C. elegans* actin encoding genes, *act-2*. *act-2(or295ts)* is a missense G14R mutation near the conserved ATP-binding pocket, which causes abnormal actin distribution (Willis et al., 2006). We found that both *pod-1(RNAi)* and *act-2(or295ts)* resulted in more symmetric contractile ring closure (Figure 3E-G). In contrast, knockdown of the Arp2/3 complex did not affect cytokinesis asymmetry, consistent with a previous report in compressed embryos (Chan et al., 2019). Ring eccentricity has been shown to be insensitive to the

reduction of myosin activity (Maddox et al., 2007). Consistently, the knockdown of LET-502/Rho kinase did not cause unilateral cytokinesis defects (Figure 3E-G). However, a strong reduction in myosin activity by the knockdown of myosin light chain MLC-4 resulted in symmetric closure (Figure 3E, G). Thus, regulation of both actin and myosin is required for unilateral cytokinesis.

Compression of the lagging cortex along the circumferential axis of the contractile ring in P_0 cells

We hypothesized that the cell cortex with asymmetric actin alignment underwent anisotropic contraction. To test this hypothesis, we measured cortical flow using particle image velocimetry (PIV) (Thielicke and Sonntag, 2021) (Figure 4A). We analyzed the maximum projection of the top 15 slices seen from the leading, lateral, and lagging cortices of embryos expressing NMY-2::GFP (Movie S2, Figure S3). To quantify cortical dynamics, we calculated the convergence of PIV vectors per area along the ring and perpendicular axes (Figure 4B). This represents an advantage of uncompressed imaging since previous studies did not report ring axis convergence, presumably due to the compression-dependent cortical rotation. Positive and negative convergence indicated the influx and efflux of cortical material per unit area, respectively (Figure 4B: arrows, cortical flow; boxes, unit area). It is important to note that cortical convergence can be interpreted as cortical compression before furrow ingression (Figure 4C, left). After furrow ingression onset, convergence indicates both compression and ingression (cortical material moving away vertically from the imaging plane) (Figure 4C, right). We used the lateral cortex view to produce average flow vector and convergence maps (Figure 4D and

Movie S3) and the leading and lagging cortex views to quantify convergence at the cell equator (Figure 4E).

First, we compared perpendicular axis convergence between leading and lagging cortices (Figure 4D, bottom row; Figure 4E, left graph; Movie S3). Before and until 11 sec following cytokinesis onset, perpendicular-axis convergence was positive at both the leading and lagging cortices, indicating that they are being compressed symmetrically along this axis (Figure 4D and E, -75–11 sec). At 16 sec after cytokinesis onset, perpendicular axis convergence started to increase at the leading cortex, owing to compression and ingression (Figure 4D and 4E, 16–84 sec). These results are in agreement with those from slightly compressed embryos (Khaliullin et al., 2018). The same study showed that the contractile ring pulls on the cortical surface from a relatively polar area at a rate proportional to the amount of ring myosin. Consistently, the elevation of the perpendicular-axis convergence at the lagging cortex coincides with its ingression-onset (Figure 4E; left graph). Because initial asymmetry in perpendicular axis convergence emerged after cytokinesis onset, it is less likely to be an ingression symmetry-breaking cue.

Next, we compared ring axis convergence between the leading and lagging cortices. We found that it was higher at the lagging cortex before cytokinesis onset, with positive convergence persisting until after furrow ingression onset of the lagging cortex (Figure 4E; right graph, -75–125sec, and Figure 4F). These results suggest that the lagging equatorial cortex is compressed along the contractile-ring axis in P_0 cells. The ring-axis compression at the lagging cortex may be specified by the biased F-actin orientation along the ring axis, while we do not claim causal relationships.

1

2 **Ring axis compression limits cleavage furrow ingression in P_0 cells**

3 Positive ring-axis cortical convergence was observed in the lagging cortex before and
4 during cytokinesis. Thus, we hypothesized that ring-axis cortical compression inhibits
5 furrow ingression during cytokinesis. To test this, we employed the *act-2(or295ts)*
6 mutant, which occasionally exhibits the ring oscillation phenotype (67%, n = 15) while
7 retaining the normal contractile ring closure rate (Figure 5A). We found that *act-*
8 *2(or295ts)* exhibited higher cortical contractility than the control, as determined by the
9 pronounced repetition of coalescence and dissipation of myosin clusters (Figure 5B). We
10 then compared the relationship between cortical compression and furrow ingression using
11 the maximum projection image of the focal planes closest to the objective lens (Figure 5C
12 and 5D, top surface) and the ring en face view (Figure 5C and 5E) from the same
13 embryo. We found that contraction at the top surface coincided with the immobilization
14 of the top furrow (Figure 5D-F; 73–84 sec and 106–117sec; Movie S4). In contrast,
15 cortical relaxation coincided with furrow ingression from the top (Figure 5D-F, 95 sec;
16 Movie S4). We measured the correlation between ring velocity and ring convergence
17 (Figure 5G, time series of one sample; Figure 5H, five embryos). We found that
18 perpendicular axis convergence did not correlate with ring ingression. In contrast, ring
19 axis convergence was negatively correlated with ring ingression from the top surface
20 (Figure 5G-H). These results suggest that local ring-axis compression locally inhibits
21 furrow ingression without affecting the rate of overall ring constriction.

22 Theoretical and experimental studies have shown that the contractile ring, with its
23 higher cortical tension, pulls in the cell cortex from the more relaxed polar region (Bray

and White, 1988; Greenspan, 1978; Khaliullin et al., 2018; Wolpert, 1960; Zinemanas and Nir, 1987, 1988). Thus, we hypothesized that the ingression rate is determined by a tug-of-war between cortical compression and contractile ring-dependent cell cortex pulling. To test this, we measured myosin cluster displacement with respect to the timing of peak compression (Figure 5I). We found that cortical myosin underwent isotropic contraction while migrating toward the furrow during relaxation (Figure 5I, left two panels). After cytokinesis, myosin clusters did not show biased movement toward the furrow (Figure 5I, right panel). The similar negative correlation between ring-axis convergence and the furrow-directed cortical flow is also observed at the lagging cortex of wild-type embryos (Figure 5D, 33 sec; Figure 5E, 0–75 sec). These results suggest that cortical compression inhibits furrow ingression by suppressing furrow-directed cortical flow at the lagging cortex.

Adhesion leads to resistance of cleavage furrow ingression in AB cells

Next, we investigated the mechanisms underlying unilateral AB cytokinesis. First, we tested whether different molecular mechanisms are required in AB cells than in P_0 cells. We tested *act-2(or295ts)*, *ani-1(RNAi)*, and *pod-1(RNAi)*, all of which resulted in symmetric P_0 cytokinesis (Figure 3B). Interestingly, the contractile rings underwent eccentric closure in all three conditions, with proximity to the cell-cell boundary as in wild-type controls (Figure 6A). Although *pod-1(RNAi)* embryos exhibited the lowest ring eccentricity in P_0 cells (Figure 3G), they exhibited wild-type level eccentricity in AB cells (Figure 6B, C). These results suggest that AB unilateral cytokinesis is not sensitive to alternations in actin dynamics and is regulated by a different mechanism.

The AB cell underwent symmetric cytokinesis after removing the neighboring P_1 cell (Figure 1). There are two possible mechanisms underlying this type of unilateral cytokinesis. First, junctional proteins may suppress furrow ingression from the lagging cortex by controlling downstream intracellular signaling (e.g., RhoA inhibition). Second, adhesion may prevent furrow ingression mechanically. We tested the latter possibility using protein-free adhesive polystyrene beads.

We attached one or two adhesive beads to the isolated AB cell before anaphase onset to test the effects of different adhesion strengths on the contractile ring dynamics. After attaching one adhesive bead, the AB contractile ring initially underwent symmetric closure but gradually increased eccentricity in the middle of cytokinesis (Figure 6C-D). The contractile ring eventually returned to the cell center by the end of ring closure (Figure 6C, right graph; 6D). When attaching two adhesive beads, the contractile ring also initially underwent symmetric closure, but ring eccentricity steadily increased until the end of cytokinesis (Figure 6C and 6E). The dynamics in the AB cells attached by two beads were similar to that of intact AB cells, wherein the ring initially closed symmetrically but later steadily increased eccentricity until it plateaued (Figure 6B). These results suggest that adhesion is sufficient to induce unilateral cytokinesis. We also found that ring eccentricity was higher when a bead was attached to the equatorial cortex rather than in the polar region (Figure 6F). Because the polar cortex undergoes relaxation and actively loses actomyosin (Chapa-Y-Lazo et al., 2020), these data suggest the importance of physical connectivity between adhesion, the plasma membrane, and the cell cortex for the regulation of furrow ingression.

Finally, we measured angles of ingression at sites with and without an adhesive bead, to assess the mechanical resistance of the cell cortex (Figure 6G). Ingression angles were initially symmetric (Figure 6G, i). As the ring constricted, the angle of ingression became overtly asymmetric, with higher and slower reduction rates at the adhesion-free and adhering sites, respectively (Figure 6G, ii). When the ring further constricts, the cell surface near it was locally detached from the adhesion site, leading to a rapid decrease in the angle of ingression (Figure 6G, iii). These dynamics suggest three stages of the adhesion-cortex relationship. First, adhesion imposes weak resistance against ring-dependent cortex bending during the initial concentric closure observed in intact embryos and in all *in vitro* experiments (Figure 6G, schematic i). Second, adhesion imposes stronger resistance as the ring constricts, leading to eccentric closure in all the tested cases (Figure 6G, schematic ii). Third, ring-dependent cell cortex pulling and a sudden adhesion rupture resulted in the quick bending of the cortex and the ring returning to the cell center when one adhesive bead was used (Figure 6G, schematic iii). Strong adhesion in intact and isolated AB cells attached by two beads prevented the premature release of ring anchoring, allowing eccentric ring positioning at the end of cytokinesis.

Adhesion limits furrow-directed cortical flow

We hypothesized that adhesion would inhibit ring-dependent cell cortex pulling. If this hypothesis is correct, the furrow-directed cortical flow should be limited by adhesion. Indeed, in our previous study on AB cell division axis orientation, we observed bead attachment-dependent suppression of furrow-directed cortical flow (Sugioka and Bowerman, 2018). However, in previous experiments, we did not rule out the possibility

that physical contact, rather than adhesion, limits furrow-directed cortical flow. Therefore, we measured furrow-directed cortical flow in the regions distal and proximal to the bead contact site using beads of different sizes (Figure 7A). The bigger the bead diameter, the larger the adhesion area and the number of adhesion bonds. We found that furrow-directed cortical flow was reduced at the cortex proximal to the contact site in a bead diameter-dependent manner (Figure 7B, C). Taken together, these results indicate that adhesion limits furrow-directed cortical flow by suppressing ring-dependent cell cortex pulling.

Discussion

Unilateral cytokinesis is widely conserved in animal development. Although spindle off-centering is a known symmetry-breaking cue for unilateral cytokinesis in ctenophore zygotes and manipulated sea urchin embryos (Bement et al., 2005; Rappaport and Conrad, 1963; Yatsu, 1912), the mechanism underlying spindle-independent symmetry breaking was unclear before this study. The two important model systems, i.e., *C. elegans* P_0 and *Drosophila* epithelial cells, have very distinct molecular requirements: the former is adhesion-independent but anillin-septin-dependent, while the latter is adhesion-dependent but anillin-septin-independent (reviewed in (Sugioka, 2021). In this study, we identified adhesion-dependent unilateral cytokinesis in *C. elegans* AB cells and performed a comparative analysis of adhesion-dependent and adhesion-independent unilateral cytokinesis.

Based on our analyses, we propose a unified symmetry-breaking mechanism underlying adhesion-independent and adhesion-dependent unilateral cytokinesis (Figure

7D). Since both ring-axis compression and adhesion suppressed the furrow ingression as well as furrow-directed cortical flow, it is likely that they inhibited ring-dependent cortex pulling (Figure 7D, middle box). During migration from the cell surface into the division plane, the cell cortex changes its curvature (Figure 7D, top-right diagrams). Ring-axis compression likely increases cortical stiffness by requiring more energy for the ring to deform and pull in the cell cortex. In contrast, adhesion externally inhibits ring-dependent cortex pulling by imposing mechanical resistance. Adhesion also induces myosin inhibition in this cell type and may prevent furrow-directed cortical flow (Sugioka and Bowerman, 2018). This mechanical suppression model is consistent with that proposed for *Drosophila* embryonic epithelial cells (Guillot and Lecuit, 2013), but our study further characterized the spatiotemporal ring-cortex interaction and expanded its utility to nonadhesive and nonepithelial cells. In summary, our findings indicate that intrinsic and extrinsic regulation of local cortical stiffness is a symmetry-breaking cue for distinct modes of spindle geometry-independent unilateral cytokinesis.

This intrinsic and extrinsic control of local cortical stiffness can explain the distinct contractile ring trajectories observed *in vivo* and *in vitro* (Figure 7D, bottom-right panels). In P_0 cells, the cell cortex is already stiffer than the other areas before cytokinesis onset (preconditioning), leading to maximum eccentricity from the early phase of cleavage (Figure 7D, schematic i). The subsequent suppression of ring-axis compression allows lagging cortex ingression and a reduction in eccentricity (Figure 4E). The oscillatory ring trajectory in *act-2(or295ts)* is likely due to oscillatory cortical compression, as shown in Figure 5 (Figure 7D, schematic ii). In the AB cell, adhesion does not impose strong mechanical resistance at the beginning, presumably owing to the

typical strain-stress relationship of a cell-cell junction and synthetic adhesives (Esfahani et al., 2021; Gent et al., 1969), then gradually increases resistance to cause eccentric closure (Figure 7D, schematic iii). When adhesion is weak, adhesion rupture reduced ring eccentricity (Figure 7D, schematic iv). Taken together, these few simple rules can generate diverse ring trajectories; therefore, this knowledge will be useful for estimating spatial cytokinesis control in more complex tissues.

One notable difference among tissues undergoing spindle-independent unilateral cytokinesis is the spatial organization of the contractile ring. Asymmetric myosin enrichment at the leading edge has been observed in *C. elegans* P_0 and AB cells and *Drosophila* pupal dorsal thorax epithelial cells (this study; (Founounou et al., 2013; Herszterg et al., 2013; Maddox et al., 2007) but not in *Drosophila* embryonic epithelia, follicular epithelia, and pupal wing epithelia (Guillot and Lecuit, 2013; Herszterg et al., 2013; Morais-de-Sá and Sunkel, 2013). Importantly, cortical stiffness-dependent suppression of ring-dependent cortex pulling can account for the asymmetric ingression of both structurally asymmetric and symmetric contractile rings (this study; (Guillot and Lecuit, 2013). This observation is consistent with our model, in which mechanical suppression occurs upstream of compression-dependent feedback (Figure 7D). We speculate that the above-described tissues are only different in terms of their downstream myosin enrichment mechanisms: structurally asymmetric and symmetric rings rely more on compression feedback and RhoA pathways, respectively.

By integrating our results and the above discussion, we predict that the ring-dependent cortex pulling is tuned differently in different tissues to execute tissue-specific morphogenic cytokinesis. Three important parameters are the strength of compression-

dependent myosin recruitment to the ring, RhoA-dependent myosin recruitment to the ring, and cortical stiffness. Compression-dependent myosin enrichment should translate subtle cortical stiffness asymmetry into increased ingression rate difference by forming a structurally asymmetric contractile ring. For a compression-dependent feedback mechanism to effectively create a structurally asymmetric contractile ring, RhoA-dependent myosin recruitment should be limited. Conversely, excessive RhoA-dependent myosin enrichment suppresses ring-dependent mechanosensing of subtle cortical stiffness asymmetry. Understanding the tissue-specific ring-cortex relationship and its local tuning by RhoA activity or tissue mechanics is necessary to further delineate the role of cytokinesis in animal morphogenesis.

Acknowledgements

We thank Kota Mizumoto and Don Moerman for critical reading of the manuscript. Some strains used in this study were obtained from the *Caenorhabditis* Genetics Center (funded by the NIH Office of Research Infrastructure Programs; P40 OD010440). We also thank Bruce Bowerman for providing valuable advice, Chris Doe for sharing lab equipment, and the Sugioka lab members for general discussions. This work was supported by the Canadian Institutes of Health Research (Project Grant; PJT-169145), Government of Canada's New Frontiers in Research Fund (NFRFE-2019-00310), and the Health Research BC (Scholar Award; SCH-2020-0406) to K.S. C.R.H was supported by British Columbia Graduate Scholarship.

Author contributions

C.R.H.: Formal analysis, Investigation, Writing-Original Draft, Validation, Visualization. **G.S.**: Formal analysis, Investigation. **W.F.**: Formal analysis, Investigation. **J.Z.**: Formal analysis, Investigation. **K.S.**: Conceptualization, Formal analysis, Investigation, Methodology, Software, Validation, Writing-Original Draft, Writing-Review & Editing, Supervision, Funding acquisition.

Declaration of interests

The authors declare no competing interests.

STAR Methods

Key Resource Table

Provided as a separate file.

Contact for Reagent and Resource Sharing

Lead contact information:

Kenji Sugioka, Department of Zoology, University of British Columbia

sugioka@zoology.ubc.ca

Lead contact holds responsibility for responding to requests and providing reagents and information.

Experimental Model and Subject Details

All *C. elegans* strains were cultured using the standard method (Brenner, 1974). A temperature sensitive-actin mutant *act-2(or295)* was cultured at 15˚C until the L4 larval stage and incubated at 25˚C overnight before imaging. Lifeact::mKate2 strain was cultured at room temperature. The following transgenes were used: *cp13*[*nmy-2*::GFP + LoxP] (non-muscle myosin II) (Dickinson et al., 2013), *cp69*[*nmy-2*::mKate2 + LoxP] (non-muscle myosin II) (Dickinson et al., 2017), *or1940*[GFP::*sas-7*] (centriole marker) (Sugioka et al., 2017), *itIs37* (mCherry::histone H2B), *ruIs32*[*pie*-1p::GFP::H2B::*pie-1* 3'UTR + *unc-119*(+)], *sybIs2855*[*mex-5*p::lifeact::mKate2::*tbb-2* 3'UTR] (F-actin marker; made by SunyBiotech), *xsSi5*[*pie*-1p::GFP::*ani-1*(AH+PH)::*pie-1* 3'UTR + *Cbr-unc-119*(+)] (RhoA biosensor) (Tse et al., 2012).

1

2 **RNAi**

3 Feeding RNAi was performed at 25˚C using the standard method (Ahringer, 2006). For
4 control RNAi, a bacterial strain carrying an empty vector (L4440) was used. For *cyk-1*,
5 *arx-2*, *ani-1* and *let-502*, the L2 stage larvae were cultured on freshly prepared feeding
6 RNAi plates on day 1. The L4 larvae were then transferred to new feeding RNAi plates
7 on day 2 and imaged on day 3. For *pod-1* and *mlc-4*, L4 larvae were cultured on feeding
8 RNAi plates and used for imaging on the next day.

9

10 **Blastomere isolation**

11 Blastomeres were isolated as described before (Hsu et al., 2019). We cut the gravid adult
12 worms in egg salt buffer (Edgar and Goldstein, 2012) and treated them with hypochlorite
13 solution [75% Clorox (Clorox) and 2.5N KOH] for 50 seconds. After washing twice with
14 Shelton's growth medium (Shelton and Bowerman, 1996), embryos were transferred to
15 fresh Shelton's growth medium. Eggshell and permeability barrier were removed by
16 mouth pipetting with hand-drawn microcapillary tubes (10 microliters, Kimble Glass
17 Inc.). The two-cell stage eggshell-free embryos were further pipetted to remove the cell-
18 cell contact.

19

20 **Adhesive polystyrene bead preparation**

21 The detailed method is described in our previous papers (Hsu et al., 2019; Sugioka and
22 Bowerman, 2018). 10 mg carboxyl-modified polystyrene beads with diameters of 30 µm
23 (Kisker Biotech GmbH & Co.), 20 µm, 10 µm, and 4.5 µm (Polysciences) were washed

twice with 100 mM 2-(N-morpholino) ethanesulfonic acid (MES) buffer (pH6.5) and incubated with 1 mL MES buffer containing 10 mg 1-Ethyl-3-(3-dimethylaminopropyl) carbodiimide (EDAC) for 15 mins at room temperature. We washed the beads twice with phosphate buffered saline (PBS) and incubated them with 0.5 mL PBS containing 0.05 µg Rhodamine Red-X succinimidyl ester (ThermoFisher Scientific) for 5 minutes. The appropriate concentration was also determined by treating the beads with a series of serially diluted Rhodamine Red-X solution (Hsu et al., 2019). The beads were washed twice with PBS and stored in PBS at 4˚C. Adhesiveness of the beads was confirmed by attaching them to the isolated blastomere using the mouse pipette. If successful, the adhesion is firmly established and cells do not dissociate spontaneously.

Live-imaging sample preparation

To obtain embryos, gravid adults were dissected on a coverslip, in a droplet of 10-12 µl of refractive index-matching medium (30% iodixanol diluted in egg salt buffer, supplemented with 30 µm diameter plain polystyrene beads) as described before (Xiong and Sugioka, 2020). After placing the coverslip gently onto a slide glass, three edges of coverslip were sealed with petroleum jelly (Vaseline), with one edge remaining open to the air. We realized that this method improved the success rate of imaging for inexperienced users. Inexperienced users may observe cell death due to the acute compression during the sample preparation and requires training using control strains. If all the processes were performed gently, the imaging condition does not have adverse effects on the embryonic viability, as judged by the normal cell division in the next cell cycle.

Microscopy

Intact embryos were imaged using a microscope Olympus IX83 (Olympus), equipped with a spinning-disk confocal unit CSU-W1 (Yokogawa), a scientific CMOS camera Prime 95B (Photometrics), a piezoelectric stage NANO-Z (Mad City Labs), a silicon immersion objective UPLSAPO60XS2 (NA1.3, 60X; Olympus), and a beam splitter Optosplit II (Cairn Research), which is controlled by Cellsense Dimension (Olympus). A silicone immersion oil (Z81114; refractive index: 1.406 at 23˚C; Olympus) was used as an immersion medium. Samples were illuminated by diode-pumped lasers with 488 nm and 561 nm wavelengths, and the simultaneous two color-imaging was performed with 150 msec camera exposure time, 1-µm Z-step size with a total of 31 slices per frame, 5.6 sec interval, and the duration of 15 mins. Isolated blastomeres were imaged using a microscope Leica DMi8 (Leica Microsystems), equipped with a spinning-disk confocal unit CSU-W1 with Borealis (Andor Technology), dual EMCCD cameras iXon Ultra 897 (Andor Technology), and an oil-immersion PL APO objective lens (NA1.4, 63X; Leica), and controlled by Metamorph (Molecular Devices). Data in Figure 6D-G were imaged with 1.5 µm Z-step size and 15 sec intervals. Data in Figure 7 were imaged with 1.5 µm Z-step size and 10 sec intervals, with only the half volume closure to the objective lens were imaged.

Quantification of the P_0 contractile ring dynamics

Obtained 4D data were deconvoluted using a constrained iterative and advanced maximum likelihood algorithm (iteration: 5), using Olympus Cellsens software

(Olympus, Inc). Each 4D tiff stack file was processed using Fiji (Schindelin et al., 2012) (Figure S1). The deconvoluted images were processed using Gaussian blur (sigma = 2) and an image J plug-in "attenuation correction" (opening =3, reference =15) (Biot et al., 2008). A 10 µm W x 32 µm H boxed region corresponding to the contractile ring was selected and adjusted for the fluorescence intensity so that the signal will not be saturated in the next step, and rotated by 3D projection (Brightest point, interpolation on). After selecting a plane of en face ring view, the images were segmented and quantified using an Image J plug-in Morpholib J (Legland et al., 2016). The segmented contractile ring areas were measured for ring radius, ring centroid, and ring angle. The radius of the segmented area was estimated using ellipsoid fitting and derived by calculating the average of major and minor radii of the ellipsoid. Data were aligned relative to the time point first exceeded 2% ring closure. The ring trajectory images were obtained with an in-house image J macro using same data.

Quantification of the AB contractile ring dynamics

Since the AB cell undergoes rotation during its division, the precise quantification is challenging. We first selected samples undergoing unilateral cleavage roughly in parallel to the imaging plane, and corrected for cell rotation using Stackreg plug-in of Image J using chromosome signal (polar bodies were deleted using a brush tool to avoid abnormal image registration) (Thévenaz et al., 1998). The rotation-corrected images were then processed by the same pipeline used for the P_0 cell.

3D visualization and quantification of contractile ring dynamics in isolated blastomeres

The oblique view of cells in Figure 1A, Figure 6A, and Figure 6D were generated using an Image J plug-in Clear Volume (Royer et al., 2015). The analysis of the contractile ring dynamics in isolated blastomeres is challenging since the cell is rotated along different axes, and not all the planes were captured during imaging. Thus, we made en face ring view images for each time point using Clear Volume, and estimated the cell and ring contours, centroids, and diameters, by selecting more than four points along the cell and ring perimeter, respectively, using an Image J macro "Smallest Enclosing Circle" (Schindelin et al., 2012). The ring closure rate and eccentricity were calculated using the method described above for other cells. Measurements were performed three times per sample, and average values were used to mitigate the relatively higher error rate compared to the automatic segmentation method used for intact embryos.

Kymographs

Kymographs in Figure 2D were generated by stacking 1.5 µm W x 32 µm H rectangular regions at a given time along a user defined line passing the equatorial cortex or furrow using an in-house image J macro. Kymographs in Figure 5B were generated by stacking 49 µm W x 1.8 µm H boxes using Fiji (built-in function, Make Montage). Kymographs in Figure 5I were generated by stacking 11 µm W x 3.7 µm H rectangular regions corresponding to a myosin cluster. The timing is adjusted so that the peak myosin cluster intensity comes the 4th out of total 8 frames, using an in-house image J macro.

Quantification of centrosome positioning

For the P_0 cell, obtained 4D images were rotated so that the angle of unilateral closure, at 5% ring closure, is accurately in parallel to the imaging plane (Figure S2A). The distances between a centrosome and leading and lagging cortices were measured using an in-house image J macro. For the AB cell, we only used samples undergoing unilateral cleavage roughly in parallel to the imaging plane (Figure S2A). The distance between a centrosome and a line passing the both ends of the AB-P_1 cell boundary was measured to calculate the centrosome-lagging cortex distance. We then drew a line passing a centrosome, and being perpendicular to the above-described AB-P_1 boundary line. The intersection of this line and a line in parallel to the leading cortex was used to calculate the centrosome-leading cortex distance. Data were aligned relative to cytokinesis onset defined by the 4D ring dynamics data described above.

Quantification of signal intensities

To accurately measure the signal intensities within a thin layer of leading and lagging cortices, we selected embryos undergoing unilateral furrow ingression roughly in parallel to the imaging plane (Figure S2B). We selected a Z slice containing the center of contractile ring at about 200 second after cytokinesis onset, and calculated the summation of three Z slices around the ring center. We then measured signal intensities in 1.83 μm x 0.55 μm boxes, corresponding to the cell cortex and the tip of the cleavage furrow before and after cleavage onset, respectively.

Quantification of the F-actin alignment

The obtained 4D data sets of lifeact::mKate2-expressing embryos were deconvoluted and analyzed to quantify ring closure dynamics by the above-described method using Morpholib J. We selected embryos showing leading or lagging cell cortex closest to the objective lens. For each data, ten slices at the cell surface closer to the objective lens were flattened by summation using Fiji, and central 9 µm x 9 µm rectangular regions were analyzed to avoid deformation of filament structure at the high-curvature surface. The orientations of actin filaments were estimated based on the gradient structure tensor in a local area using an Image J plug-in Orientation J (Gradient: Cubic Spline, local window: 2 pixel) (Püspöki et al., 2016). Circular mean was calculated using Scipy (Virtanen et al., 2020) and the timings of data were aligned relative to cytokinesis onset.

Visualization of F-actin alignment

To visualize F-actin alignment in Figure 3A-B, the above-described flattened images were processed using an unsharp mask (Image J built-in function) and an Image J plug-in Feature J (Edges:, smoothing scale 1.0) (Meijering). The orientation vectors in Figure 3B were generated using Orientation J.

Particle Image Velocimetry

A detailed image preprocessing pipeline is shown in Figure S3. Briefly, 4D data sets of NMY-2::GFP and GFP::-SAS-7-expressing embryos were processed with Gaussian Blur (sigma =1) and unsharp mask (radius =1, mask = 0.6) using Fiji. Centriole signals were deleted by filling zero values. After intensity adjustment to avoid signal saturation, half volume of image stack was filled with zero values to avoid projecting cortical myosin

from opposite cortical sides. Obtained images were projected using an Image J function "3D projection." We rotated 3D projected data relative to angle of cleavage at 5% closure and generated leading, lagging, and lateral cortex views. Note that not always both lagging and leading cortices were clearly visible, so that in some embryos, either the leading or lagging cortex was used. Using these flattened cell cortex images, Particle Image Velocimetry was performed using MATLAB software PIV LAB (Algorithm: FFT window deformation, Interrogation area: 5.8 µm, Step size: 2.9 µm, Sub-pixel estimator: Gauss 2x3 point, Correlation robustness: Standard) (Thielicke and Sonntag, 2021). We rejected vectors exceeding 0.25 µm/sec to remove estimation errors (the setting was visually confirmed to reflect the myosin foci movement). Obtained 3D matrix data (2D x time) were used for downstream analyses. The PIV matrix data were aligned relative to cytokinesis onset, centered relative to the cell center corresponding to the furrow position, and resized to contain an entire embryo using Numpy and Pandas (Harris et al., 2020; McKinney, 2010). Mean PIV vectors were calculated and plotted using Matplotlib (stream plot) (Hunter, 2007).

Estimation of cortical convergence

Cortical convergence was derived using the PIV vector matrix and a NumPy gradient function (Harris et al., 2020). When we define perpendicular-axis and ring-axis cortical flow velocities in an i x j matrix as $u_{i,j}$ and $v_{i,j}$, respectively, $u_{i+h,j}$, $u_{i-h,j}$, $v_{i,j+h}$, $v_{i,j-h}$ can be defined as follows using Taylor series (Quarteroni et al., 2010):

$$u_{i+h,j} = u_{i,j} + h\frac{\partial u_{i,j}}{\partial i} + \frac{h^2}{2!}\frac{\partial^2 u_{i,j}}{\partial i^2} + \mathcal{O}(h^3) \qquad (4)$$

$$u_{i-h,j} = u_{i,j} - h\frac{\partial u_{i,j}}{\partial i} + \frac{h^2}{2!}\frac{\partial^2 u_{i,j}}{\partial i^2} + \mathcal{O}(h^3) \qquad (5)$$

$$v_{i,j+h} = v_{i,j} + h\frac{\partial v_{i,j}}{\partial j} + \frac{h^2}{2!}\frac{\partial^2 v_{i,j}}{\partial j^2} + \mathcal{O}(h^3) \qquad (6)$$

$$v_{i,j-h} = v_{i,j} - h\frac{\partial v_{i,j}}{\partial j} + \frac{h^2}{2!}\frac{\partial^2 v_{i,j}}{\partial j^2} + \mathcal{O}(h^3) \qquad (7)$$

And we will obtain the followings by subtraction:

$$u_{i+h,j} - u_{i-h,j} = 2h\frac{\partial u_{i,j}}{\partial i} + \mathcal{O}(h^3) \qquad (8)$$

$$V_{i,j+h} - V_{i,j-h} = 2h\frac{\partial v_{i,j}}{\partial j} + \mathcal{O}(h^3) \qquad (9)$$

Thus, the cortical flow gradients at the interior points can be defined as follows:

$$\frac{\partial u_{i,j}}{\partial i} = \frac{u_{i+h,j} - u_{i-h,j}}{2h} + \mathcal{O}(h^2) \approx \frac{u_{i+h,j} - u_{i-h,j}}{2h} \qquad (10)$$

$$\frac{\partial V_{i,j}}{\partial j} = \frac{v_{i,j+h} - v_{i,j-h}}{2h} + \mathcal{O}(h^2) \approx \frac{v_{i,j+h} - v_{i,j-h}}{2h} \qquad (11)$$

At the boundary, first order one-sided differences were achieved as follows:

$$\frac{\partial u_{i,j}}{\partial i} = \frac{u_{i+h,j} - u_{i,j}}{h} + \mathcal{O}(h) \approx \frac{u_{i+h,j} - u_{i,j}}{h} \qquad (12)$$

$$\frac{\partial v_{i,j}}{\partial j} = \frac{v_{i,j+h} - v_{i,j}}{h} + \mathcal{O}(h) \approx \frac{v_{i,j+h} - v_{i,j}}{h} \qquad (13)$$

Perpendicular-axis and ring-axis cortical convergence $p_{i,j}$, $q_{i,j}$, respectively, were calculated as follows, where *a* is the PIV step size:

$$p_{i,j} = -\frac{1}{a}\frac{\partial u_{i,j}}{\partial i} \approx -\frac{1}{a}\frac{\left(u_{i+1,j} - u_{i-1,j}\right)}{2} \qquad (at\ the\ interior\ points) \quad (14)$$

$$p_{i,j} = -\frac{1}{a}\frac{\partial u_{i,j}}{\partial i} \approx -\frac{1}{a}\left(u_{i\pm1,j} - u_{i,j}\right) \qquad (at\ the\ boundary) \quad (15)$$

$$q_{i,j} = -\frac{1}{a}\frac{\partial v_{i,j}}{\partial j} \approx -\frac{1}{a}\frac{\left(v_{i,j+1} - v_{i,j-1}\right)}{2} \quad (at\ the\ interior\ points) \quad (16)$$

$$q_{i,j} = -\frac{1}{a}\frac{\partial v_{i,j}}{\partial j} \approx -\frac{1}{a}\left(v_{i,j\pm1} - v_{i,j}\right) \quad (at\ the\ boundary) \quad (17)$$

Mean convergence of embryos was calculated for each grid, and plotted in Figure 4D using Matplotlib (stream plot). To quantify leading and lagging cortex convergence at the equatorial region in Figure 4E, we calculated mean convergence within a 6x3 grid (14.6 μm W x 5.9 μm H) around the center of the furrow position.

Myosin foci tracking

Before the analysis of myosin foci, cell position was registered using image J plug-in Stackreg, to eliminate the movement of myosin foci caused by the movement of cell body. Myosin foci in Figure 7B were tracked using Manual Tracking plug-in of Image J.

Statistical analysis

For multiple comparisons, one-way ANOVA with the Holm-Sidak's method was used. The comparison of two data was performed using the Mann-Whitney U-test or Welch's t-test. No statistical method was used to predetermine the sample size. Error bars or bands are corresponding to the 95% confidence interval. Pearson's coefficients were calculated in multiple 95 sec windows in Figure 5G. In Figure 5I, a 95 sec window corresponding to the ring oscillation period was used. The experiments were not randomized. The investigators were not blinded to the study. Statistical analyses were performed using either SciPy or Prism 9 (Graphpad). Symbols such as "****", "***", "**", and "*" indicate $p < 0.0001$, $p < 0.001$, $p < 0.01$, and $p < 0.05$, respectively.

Figure legends

Figure 1. Intrinsic and extrinsic control of unilateral cytokinesis in *C. elegans* embryos.

(**A**) Eccentric and concentric contractile ring closure of *C. elegans* embryonic blastomeres shown by volumetric 4D imaging of NMY-2::GFP (green, non-muscle myosin II), GFP::SAS-7 (green, centriole) and histone H2B::mCherry (magenta, chromosome) in the zygote P_0, 2-cell stage AB, and isolated AB. In this and subsequent figures, anterior and posterior are to the left and right, respectively. (**B**) Trajectory of ring constriction. Outlines of the contractile ring during cytokinesis are plotted for single P_0, AB, and isolated AB cells. Color coding indicates time relative to cytokinesis onset. (**C**) Mean ring closure and eccentricity. Times are relative to cytokinesis onset. Error bands indicate 95% confidence intervals. Scale bars, 10 μm.

Figure 2. Mitotic spindle positioning, RhoA activity, and myosin enrichment are not asymmetric at the beginning of the P_0 and AB cytokinesis.

(**A**) Contractile ring assembly mechanism in *C. elegans* zygotes. (i) Mitotic spindle positioning determines the active RhoA zone where centralspindlin activates ECT-2-RhoGEF and RhoA; RhoA-GTP then activates myosin and actin assembly ("RhoA pathway"). (ii) At the cell surface, cortical flow compresses the equatorial cell cortex, producing actin alignment and myosin enrichment. Ring constriction further pulls the cell cortex to induce pole-to-equator cortical flow to form a positive feedback loop ("compression-feedback pathway"). (**B, C**) Centrosome positions relative to the axis of

contractile ring constriction. LE and LG indicate distances between the centrosome and cell cortex, respectively. (**D**) Kymographs of myosin and active RhoA localization at the equatorial cell cortex (ROI shown in B) using intensity-based color-coding. (**E**) Ratios of myosin and active RhoA signal intensities between leading and lagging cortices. Times are relative to cytokinesis onset. Error bands and bars indicate 95% confidence intervals. Scale bars, 10 μm.

Figure 3. Actin alignment asymmetry specifies leading and lagging cell cortices of P_0 cells.

(**A**) F-actin distribution in leading and lagging cortices at 50 seconds before cytokinesis onset. White dotted boxes show F-actin alignments in B. Bottom panels show edge-enhanced images. (**B**) F-actin orientation at leading and lagging cell cortices. Yellow lines in the second and fourth columns indicate estimated F-actin orientations. Each box is 12 × 9 μm. (**C**) Circular means of F-actin orientation during P_0 cytokinesis. (**D**) Ratios of F-actin intensities between leading and lagging cortices. (**E**) Contractile ring trajectories after perturbation of key actin and myosin regulators. (**F**) Mean ring closures and eccentricities. Control data are the same as for Fig. 1C. (**G**) Eccentricities at 50% ring closure. Times are relative to cytokinesis onset. Error bands and bars indicate 95% confidence intervals. P-values were calculated using one-way ANOVA followed by Holm-Sidak's multiple comparison test. Scale bars, 10 μm.

Figure 4. Lagging equatorial cortex is compressed along the contractile ring axis in P_0 cells.

(**A**) Cortical flow of a single embryo visualized from multiple angles. Yellow arrows indicate the movement of myosin foci from particle image velocimetry. (**B, C**) Concept of cortical convergence. Net influx and efflux of cortical flow within a certain area were calculated for the axes in parallel and perpendicular to the contractile ring (B). Cortical convergence indicates the degree of cortex compression before cleavage onset. After cleavage onset, convergence indicates both compression and the loss of cell surface from the focal plane due to invagination (C). (**D**) Mean cortical convergences and cortical flows calculated using the lateral cortex view. Arrow size scales with the cortical flow velocity. Convergence in the local area is shown by the color code. Dotted boxes indicate the equatorial regions of leading (top) and lagging (bottom) cortices. (**E**) Mean convergences at equator (boxes in schematic) calculated using leading and lagging cortex views. (**F**) Ring-axis convergences before cytokinesis onset. P-values were calculated by the Mann-Whitney U-test. Times are relative to cytokinesis onset. Error bands and bars indicate 95% confidence intervals. Scale bars, 10 μm.

Figure 5. Ring axis compression inhibits the furrow ingression and furrow-directed cortical flow.

(**A**) Contractile ring trajectory of a single *act-2(or295ts)* mutant (left panel) and the average of ten embryos (graph). (**B**) Kymographs of the cortical NMY-2::GFP with intensity-based color coding. (**C**) Planes shown in (D-F). (**D**) NMY-2::GFP localization at the top surface during cytokinesis. Yellow and light blue dotted circles indicate the area exhibiting contraction and relaxation, respectively. (**E**) Ring en face view of the same embryo shown in panel D. Dotted lines indicate top and bottom limits of the

contractile ring. Arrows indicate the movement of the ring limit. (**F**) Ring trajectories of the contractile ring shown in (E). Top- and bottom-oriented movements are shown in yellow and blue, respectively. (**G**) Relationship between ring velocity and cortical convergence. Ring centroid velocities of one embryo were plotted with ring axis convergences at the top surface. Positive ring velocity represents ring ingression from the top and vice versa. Pearson's correlation coefficients in 95 sec windows are also shown. (**H**) Pearson's correlation coefficients between ring velocity and cortical convergence from five embryos. (**I**) Furrow-directed movement of myosin clusters during relaxation. Kymographs of individual and averaged clusters are shown relative to the time of peak signal intensity. Except for I, times are relative to cytokinesis onset. Error bands indicate 95% confidence intervals. Scale bars, 10 μm.

Figure 6. Adhesion results in resistance of cleavage furrow ingression in AB cells. (**A**) Eccentric ring closure in AB cells. In addition to myosin II (green), cells are labeled with centriole (green) and histone-H2B (magenta), except for *act-2(or295ts)* mutants. White dotted lines indicate the AB-P_1 boundary. (**B**) Mean ring closure and eccentricity in *pod-1(RNAi)*. (**C**) Ring eccentricity in intact embryos (control vs. *pod-1(RNAi)*), and in isolated AB blastomeres with or without the attachment of adhesive beads. p-values were calculated by Welch's t-test for the left graph and one-way ANOVA with Holm-Sidak's multiple comparison test for the remaining data set. (**D, E**) Oblique view of contractile rings in the bead attached AB cell. Ring trajectory and mean eccentricity are shown in D' E' and D'' E'', respectively. (**F**) Ring eccentricity as a function of bead contact site. (**G**) Angle of ingression during adhesion-dependent unilateral cleavage. Insets in the top

panels show the ring-bead interface. The graph at the right shows angles of ingression from three experiments. Times are relative to cytokinesis onset. Error bands and bars indicate 95% confidence intervals. Scale bars, 10 μm.

Figure 7. Adhesion inhibits furrow-directed cortical flow.

(**A**) Isolated AB cells attached to adhesive beads of different diameters. (**B**) Furrow-directed cortical flow proximal (P) and distal (D) to bead attachment sites. (**C**) Myosin movement with a bead attached. Arrowheads indicate myosin foci. Arrows below micrographs indicate total displacements over 15 sec. (**D**) Working hypothesis for symmetry-breaking in unilateral cytokinesis. Ring-axis compression and cell-cell adhesion inhibit cortical ingression and furrow-directed cortical flow by suppressing ring-dependent cortex pulling (left diagram). Perpendicular-axis compression in wild-type embryos is a result of furrow-directed cortical flow that induces myosin enrichment at the equatorial cortex through compression-dependent feedback. Suppression of cell cortex pulling induces unilateral cytokinesis with and without the compression-dependent feedback. Cortical stiffness asymmetry induced by intrinsic cortical dynamics and external adhesion is the symmetry-breaking cue (right diagram). Differences in ring trajectories can be explained by differences in the timing of stiffness change (diagrams i-iv, lower right panel). Error bars indicate 95% confidence intervals. Scale bars, 10 μm. p-values were calculated by one-way ANOVA with Holm-Sidak's multiple comparison test.

Figure S1. Imaging and contractile ring analysis methods.

(**A**) Imaging conditions and analytical flow charts. For intact embryos, we used refractive index matching medium and polystyrene beads as spacers. For isolated AB blastomeres, we used a normal growth medium and a different analytical pipeline to estimate ring size and position because of the cells' movement and rotation. Isolated AB cells were measured three times, and average values were analyzed. (**B**) Temporal color-coded image of 20 frames around cytokinesis onset showing that compression-free embryos do not exhibit global cortical rotation. (**C**) Ring en face view after the rotation of 3D projected data and ring segmentation. (**D**) Contractile ring closure data after alignment of time series data relative to 2 % ring closure. Error bars indicate 95% confidence intervals.

Figure S2. Measurement of centrosome positioning and signal intensity.

(**A**) Image analysis pipelines for P0 (left) and AB (right) spindle positioning. All processes were performed semi-automatically using in-house image J macros. (**B**) Image analysis pipeline for active RhoA and myosin signal intensities. White boxes in the insets of images on the right show the areas of measurement.

Figure S3. Generation of cortical myosin data used for PIV analysis.

(A) An image preprocessing pipeline used to generate cortical myosin data for Particle Image Velocimetry analyses. See also Methods section. At the quality control step, very noisy or dim images were not selected for PIV analyses. These images are usually from image planes furthest from the objective lens.

Movie S1. Dynamics of cortical myosin and contractile ring of a single embryo

Left top: maximum projection of cell surface NMY-2::GFP. Bottom left: ring en face view of NMY-2::GFP. Bottom middle: segmented ring. Bottom right: reconstructed ring trajectory. Right graph: Contractile ring dynamics of the same embryo. Note that an identical embryo was used to generate all data.

Movie S2. Cortical flow and flow vector map using Particle Image Velocimetry

The cell surface NMY-2::GFP of leading (left), lateral (middle), and lagging cortex views (right). Yellow arrows are generated by Particle Image Velocimetry. Times are relative to cytokinesis onset.

Movie S3. Average cortical flow and convergence map using lateral view

Perpendicular-axis (left) and ring-axis convergences (right) are shown. The color code is the same as Figure 4D (warm colors: positive, cool colors: negative values). Times are relative to cytokinesis onset.

Movie S4. Dynamics of cortical compression and cortical ingression

Cell surface (top) and ring en face view (bottom left) of NMY-2::GFP. Ring outlines and centroid trajectory were color coded as in Figure 5F (yellow: movement towards the contraction site, blue: movement away from the relaxation site).

References

Ahringer, J. (2006). Reverse genetics. WormBook https://doi.org/10.1895/wormbook.1.47.1.

Basant, A., and Glotzer, M. (2018). Spatiotemporal Regulation of RhoA during Cytokinesis. Curr. Biol. *28*, R570–R580. .

Basant, A., Lekomtsev, S., Tse, Y.C., Zhang, D., Longhini, K.M., Petronczki, M., and Glotzer, M. (2015). Aurora B kinase promotes cytokinesis by inducing centralspindlin oligomers that associate with the plasma membrane. Dev. Cell *33*, 204–215. .

Bement, W.M., Benink, H.A., and von Dassow, G. (2005). A microtubule-dependent zone of active RhoA during cleavage plane specification. J. Cell Biol. *170*, 91–101. .

Biot, E., Crowell, E., Hofte, H., Maurin, Y., Vernhettes, S., and Andrey, P. (2008). A new filter for spot extraction in n-dimensional biological imaging. In 2008 5th IEEE International Symposium on Biomedical Imaging: From Nano to Macro, pp. 975–978.

Bourdages, K.G., Lacroix, B., Dorn, J.F., Descovich, C.P., and Maddox, A.S. (2014). Quantitative analysis of cytokinesis in situ during C. elegans postembryonic development. PLoS One *9*, e110689. .

Bray, D., and White, J.G. (1988). Cortical flow in animal cells. Science *239*, 883–8. .

Brenner, S. (1974). The genetics of Caenorhabditis elegans. Genetics *77*, 71–94. .

Chan, F.-Y., Silva, A.M., Saramago, J., Pereira-Sousa, J., Brighton, H.E., Pereira, M., Oegema, K., Gassmann, R., and Carvalho, A.X. (2019). The ARP2/3 complex prevents excessive formin activity during cytokinesis. Mol. Biol. Cell *30*, 96–107. .

Chapa-Y-Lazo, B., Hamanaka, M., Wray, A., Balasubramanian, M.K., and Mishima, M. (2020). Polar relaxation by dynein-mediated removal of cortical myosin II. J. Cell Biol. *219*. https://doi.org/10.1083/jcb.201903080.

Dickinson, D.J., Ward, J.D., Reiner, D.J., and Goldstein, B. (2013). Engineering the Caenorhabditis elegans genome using Cas9-triggered homologous recombination. Nat. Methods *10*, 1028–1034. .

Dickinson, D.J., Schwager, F., Pintard, L., Gotta, M., and Goldstein, B. (2017). A Single-Cell Biochemistry Approach Reveals PAR Complex Dynamics during Cell Polarization. Dev. Cell *42*, 416-434.e11. .

Douglas, M.E., Davies, T., Joseph, N., and Mishima, M. (2010). Aurora B and 14-3-3 coordinately regulate clustering of centralspindlin during cytokinesis. Curr. Biol. *20*, 927–933. .

Edgar, L.G., and Goldstein, B. (2012). Culture and Manipulation of Embryonic Cells. Methods Cell Biol. *107*, 151–175. .

Esfahani, A.M., Rosenbohm, J., Safa, B.T., Lavrik, N.V., Minnick, G., Zhou, Q., Kong, F., Jin, X., Kim, E., Liu, Y., et al. (2021). Characterization of the strain-rate-dependent mechanical response of single cell-cell junctions. Proc. Natl. Acad. Sci. U. S. A. *118*. https://doi.org/10.1073/pnas.2019347118.

Ferguson, D.J.P. (1988). An ultrastructural study of mitosis and cytokinesis in normal 'resting' human breast. Cell Tissue Res. *252*, 581–587. .

Fleming, E.S., Zajac, M., Moschenross, D.M., Montrose, D.C., Rosenberg, D.W., Cowan, A.E., and Tirnauer, J.S. (2007). Planar spindle orientation and asymmetric cytokinesis in the mouse small intestine. J. Histochem. Cytochem. *55*, 1173–80. .

Founounou, N., Loyer, N., and Le Borgne, R. (2013). Septins regulate the contractility of the actomyosin ring to enable adherens junction remodeling during cytokinesis of epithelial cells. Dev. Cell *24*, 242–255. .

Gent, A.N., Petrich, R.P., and Tabor, D. (1969). Adhesion of viscoelastic materials to rigid substrates. Proc. R. Soc. Lond. A Math. Phys. Sci. *310*, 433–448. .

Goley, E.D., and Welch, M.D. (2006). The ARP2/3 complex: an actin nucleator comes of age. Nat. Rev. Mol. Cell Biol. *7*, 713–726. .

Gómez-Cavazos, J.S., Lee, K.-Y., Lara-González, P., Li, Y., Desai, A., Shiau, A.K., and Oegema, K. (2020). A Non-canonical BRCT-Phosphopeptide Recognition Mechanism Underlies RhoA Activation in Cytokinesis. Curr. Biol. *30*, 3101-3115.e11. .

Greenspan, H.P. (1978). On fluid-mechanical simulations of cell division and movement. J. Theor. Biol. *70*, 125–134. .

Guillot, C., and Lecuit, T. (2013). Adhesion disengagement uncouples intrinsic and extrinsic forces to drive cytokinesis in epithelial tissues. Dev. Cell *24*, 227–241. .

Harris, C.R., Millman, K.J., van der Walt, S.J., Gommers, R., Virtanen, P., Cournapeau, D., Wieser, E., Taylor, J., Berg, S., Smith, N.J., et al. (2020). Array programming with NumPy. Nature *585*, 357–362. .

Herszterg, S., Leibfried, A., Bosveld, F., Martin, C., and Bellaiche, Y. (2013). Interplay between the Dividing Cell and Its Neighbors Regulates Adherens Junction Formation during Cytokinesis in Epithelial Tissue. Dev. Cell *24*, 256–270. .

Hsu, C.R., Xiong, R., and Sugioka, K. (2019). In Vitro Reconstitution of Spatial Cell Contact Patterns with Isolated Caenorhabditis elegans Embryo Blastomeres and Adhesive Polystyrene Beads. J. Vis. Exp. https://doi.org/10.3791/60422.

Hunter, J.D. (2007). Matplotlib: A 2D Graphics Environment. Comput. Sci. Eng. *9*, 90–95. .

Jinguji, Y., and Ishikawa, H. (1992). Electron microscopic observations on the maintenance of the tight junction during cell division in the epithelium of the mouse small intestine. Cell Struct. Funct. *17*, 27–37. .

Khaliullin, R.N., Green, R.A., Shi, L.Z., Gomez-Cavazos, J.S., Berns, M.W., Desai, A., and Oegema, K. (2018). A positive-feedback-based mechanism for constriction rate acceleration during cytokinesis in Caenorhabditis elegans. Elife *7*. https://doi.org/10.7554/elife.36073.

Koyama, H., Umeda, T., Nakamura, K., Higuchi, T., and Kimura, A. (2012). A high-resolution shape fitting and simulation demonstrated equatorial cell surface softening during cytokinesis and its promotive role in cytokinesis. PLoS One *7*, e31607. .

Legland, D., Arganda-Carreras, I., and Andrey, P. (2016). MorphoLibJ: integrated library and plugins for mathematical morphology with ImageJ. Bioinformatics *32*, 3532–3534. .

Li, Y., and Munro, E. (2021). Filament-guided filament assembly provides structural memory of filament alignment during cytokinesis. Dev. Cell *56*, 2486-2500.e6. .

Liu, J., Fairn, G.D., Ceccarelli, D.F., Sicheri, F., and Wilde, A. (2012). Cleavage Furrow Organization Requires PIP2-Mediated Recruitment of Anillin. Curr. Biol. *22*, 64–69. .

Maddox, A.S., Lewellyn, L., Desai, A., and Oegema, K. (2007). Anillin and the septins promote asymmetric ingression of the cytokinetic furrow. Dev. Cell *12*, 827–835. .

Matsumura, F. (2005). Regulation of myosin II during cytokinesis in higher eukaryotes. Trends Cell Biol. *15*, 371–377. .

McKinney, W. (2010). Data Structures for Statistical Computing in Python. In Proceedings of the 9th Python in Science Conference, (SciPy), p.

Meijering, E. Feature J: An Image J Plugin Suite for Image Feature Extraction.

Morais-de-Sá, E., and Sunkel, C. (2013). Adherens junctions determine the apical position of the midbody during follicular epithelial cell division. EMBO Rep. *14*, 696–703. .

Nakajima, Y.-I., Lee, Z.T., McKinney, S.A., Swanson, S.K., Florens, L., and Gibson, M.C. (2019). Junctional tumor suppressors interact with 14-3-3 proteins to control planar spindle alignment. J. Cell Biol. *218*, 1824–1838. .

van Oostende Triplet, C., Jaramillo Garcia, M., Haji Bik, H., Beaudet, D., and Piekny, A. (2014). Anillin interacts with microtubules and is part of the astral pathway that defines cortical domains. J. Cell Sci. *127*, 3699–3710. .

Otomo, T., Otomo, C., Tomchick, D.R., Machius, M., and Rosen, M.K. (2005). Structural basis of Rho GTPase-mediated activation of the formin mDia1. Mol. Cell *18*, 273–281. .

Ozugergin, I., Mastronardi, K., Law, C., and Piekny, A. (2022). Diverse mechanisms regulate contractile ring assembly for cytokinesis in the two-cell Caenorhabditis elegans embryo. J. Cell Sci. *135*. https://doi.org/10.1242/jcs.258921.

Piekny, A.J., and Glotzer, M. (2008). Anillin is a scaffold protein that links RhoA, actin, and myosin during cytokinesis. Curr. Biol. *18*, 30–36. .

Püspöki, Z., Storath, M., Sage, D., and Unser, M. (2016). Transforms and Operators for Directional Bioimage Analysis: A Survey. Adv. Anat. Embryol. Cell Biol. *219*, 69–93. .

Quarteroni, A., Sacco, R., and Saleri, F. (2010). Numerical Mathematics (Springer Science & Business Media).

Rappaport, R. (1986). Establishment of the Mechanism of Cytokinesis in Animal Cells. In International Review of Cytology, G.H. Bourne, K.W. Jeon, and M. Friedlander, eds. (Academic Press), pp. 245–281.

Rappaport, R. (1996). Division Mechanism Function and Its Consequences. In Cytokinesis in Animal Cells, (Cambridge University Press), pp. 230–264.

Rappaport, R., and Conrad, G.W. (1963). AN EXPERIMENTAL ANALYSIS OF UNILATERAL CLEAVAGE IN INVERTEBRATE EGGS. J. Exp. Zool. *153*, 99–112. .

Reymann, A.-C., Staniscia, F., Erzberger, A., Salbreux, G., and Grill, S.W. (2016). Cortical flow aligns actin filaments to form a furrow. Elife *5*, e17807. .

Royer, L.A., Weigert, M., Günther, U., Maghelli, N., Jug, F., Sbalzarini, I.F., and Myers, E.W. (2015). ClearVolume: open-source live 3D visualization for light-sheet microscopy. Nat. Methods *12*, 480–481. .

Schindelin, J., Arganda-Carreras, I., Frise, E., Kaynig, V., Longair, M., Pietzsch, T., Preibisch, S., Rueden, C., Saalfeld, S., Schmid, B., et al. (2012). Fiji: an open-source platform for biological-image analysis. Nat. Methods *9*, 676–682. .

Schonegg, S., Hyman, A.A., and Wood, W.B. (2014). Timing and mechanism of the initial cue establishing handed left–right asymmetry in Caenorhabditis elegans embryos. Genesis *52*, 572–580. .

Shelton, C.A., and Bowerman, B. (1996). Time-dependent responses to glp-1-mediated inductions in early C. elegans embryos. Development *122*, 2043–2050. .

Singh, D., Odedra, D., Dutta, P., and Pohl, C. (2019). Mechanical stress induces a scalable switch in cortical flow polarization during cytokinesis. J. Cell Sci. *132*. https://doi.org/10.1242/jcs.231357.

Somers, W.G., and Saint, R. (2003). A RhoGEF and Rho family GTPase-activating protein complex links the contractile ring to cortical microtubules at the onset of cytokinesis. Dev. Cell *4*, 29–39. .

Sugioka, K. (2021). Symmetry-breaking of animal cytokinesis. Semin. Cell Dev. Biol. https://doi.org/10.1016/j.semcdb.2021.12.008.

Sugioka, K., and Bowerman, B. (2018). Combinatorial Contact Cues Specify Cell Division Orientation by Directing Cortical Myosin Flows. Dev. Cell *46*, 257-270.e5. .

Sugioka, K., Hamill, D.R., Lowry, J.B., McNeely, M.E., Enrick, M., Richter, A.C., Kiebler, L.E., Priess, J.R., and Bowerman, B. (2017). Centriolar SAS-7 acts upstream of SPD-2 to regulate centriole assembly and pericentriolar material formation. Elife *6*, e20353. .

Tatsumoto, T., Xie, X., Blumenthal, R., Okamoto, I., and Miki, T. (1999). Human ECT2 is an exchange factor for Rho GTPases, phosphorylated in G2/M phases, and involved in cytokinesis. J. Cell Biol. *147*, 921–928. .

Taulet, N., Vitre, B., Anguille, C., Douanier, A., Rocancourt, M., Taschner, M., Lorentzen, E., Echard, A., and Delaval, B. (2017). IFT proteins spatially control the geometry of cleavage furrow ingression and lumen positioning. Nat. Commun. *8*, 1928. .

Thévenaz, P., Ruttimann, U.E., and Unser, M. (1998). A pyramid approach to subpixel registration based on intensity. IEEE Trans. Image Process. *7*, 27–41. .

Thieleke-Matos, C., Osório, D.S., Carvalho, A.X., and Morais-de-Sá, E. (2017). Emerging Mechanisms and Roles for Asymmetric Cytokinesis. Int. Rev. Cell Mol. Biol. *332*, 297–345. .

Thielicke, W., and Sonntag, R. (2021). Particle Image Velocimetry for MATLAB: Accuracy and enhanced algorithms in PIVlab. J. Open Res. Softw. *9*, 12. .

Tse, Y.C., Werner, M., Longhini, K.M., Labbe, J.-C., Goldstein, B., and Glotzer, M. (2012). RhoA activation during polarization and cytokinesis of the early Caenorhabditis elegans embryo is differentially dependent on NOP-1 and CYK-4. Mol. Biol. Cell *23*, 4020–4031. .

Virtanen, P., Gommers, R., Oliphant, T.E., Haberland, M., Reddy, T., Cournapeau, D., Burovski, E., Peterson, P., Weckesser, W., Bright, J., et al. (2020). SciPy 1.0: fundamental algorithms for scientific computing in Python. Nat. Methods *17*, 261–272. .

Vogetseder, A., Karadeniz, A., Kaissling, B., and Le Hir, M. (2005). Tubular cell proliferation in the healthy rat kidney. Histochem. Cell Biol. *124*, 97–104. .

Willis, J.H., Munro, E., Lyczak, R., and Bowerman, B. (2006). Conditional dominant mutations in the Caenorhabditis elegans gene act-2 identify cytoplasmic and muscle roles for a redundant actin isoform. Mol. Biol. Cell *17*, 1051–1064. .

Wolpert, L. (1960). The mechanics and mechanism of cleavage. Int. Rev. Cytol. *10*, 163–216. .

Woolner, S., and Papalopulu, N. (2012). Spindle position in symmetric cell divisions during epiboly is controlled by opposing and dynamic apicobasal forces. Dev. Cell *22*, 775–787. .

Xie, C., Jiang, Y., Zhu, Z., Huang, S., Li, W., and Ou, G. (2021). Actin filament debranching regulates cell polarity during cell migration and asymmetric cell division. Proc. Natl. Acad. Sci. U. S. A. *118*. https://doi.org/10.1073/pnas.2100805118.

Xiong, R., and Sugioka, K. (2020). Improved 3D cellular morphometry of Caenorhabditis elegans embryos using a refractive index matching medium. PLoS One *15*, e0238955. .

Yatsu, N. (1912). Observations and experiments on the ctenophore egg. Jour. Coll. Sci. Tokyo *32*, 1–21. .

Yüce, O., Piekny, A., and Glotzer, M. (2005). An ECT2-centralspindlin complex regulates the localization and function of RhoA. J. Cell Biol. *170*, 571–82. .

Ziegler, H.E. (1903). Experimentelle studien über zelltheilung. IV. Die zelltheilung der furchungzellen bei Beroe und Echinus. Archiv Für Entwicklungsmechanik Der Organismen *16*, 155–175. .

Zinemanas, D., and Nir, A. (1987). Fluid Mechanical Simulations of Cell Furrowing Due to Anisotropic Surface Forces. In Biomechanics of Cell Division, N. Akkas, ed. (Boston, MA: Springer US), pp. 281–305.

Zinemanas, D., and Nir, A. (1988). On the viscous deformation of biological cells under anisotropic surface tension. J. Fluid Mech. *193*, 217–241. .

Figure 1 (Hsu, Sangha, Fan, et al.)

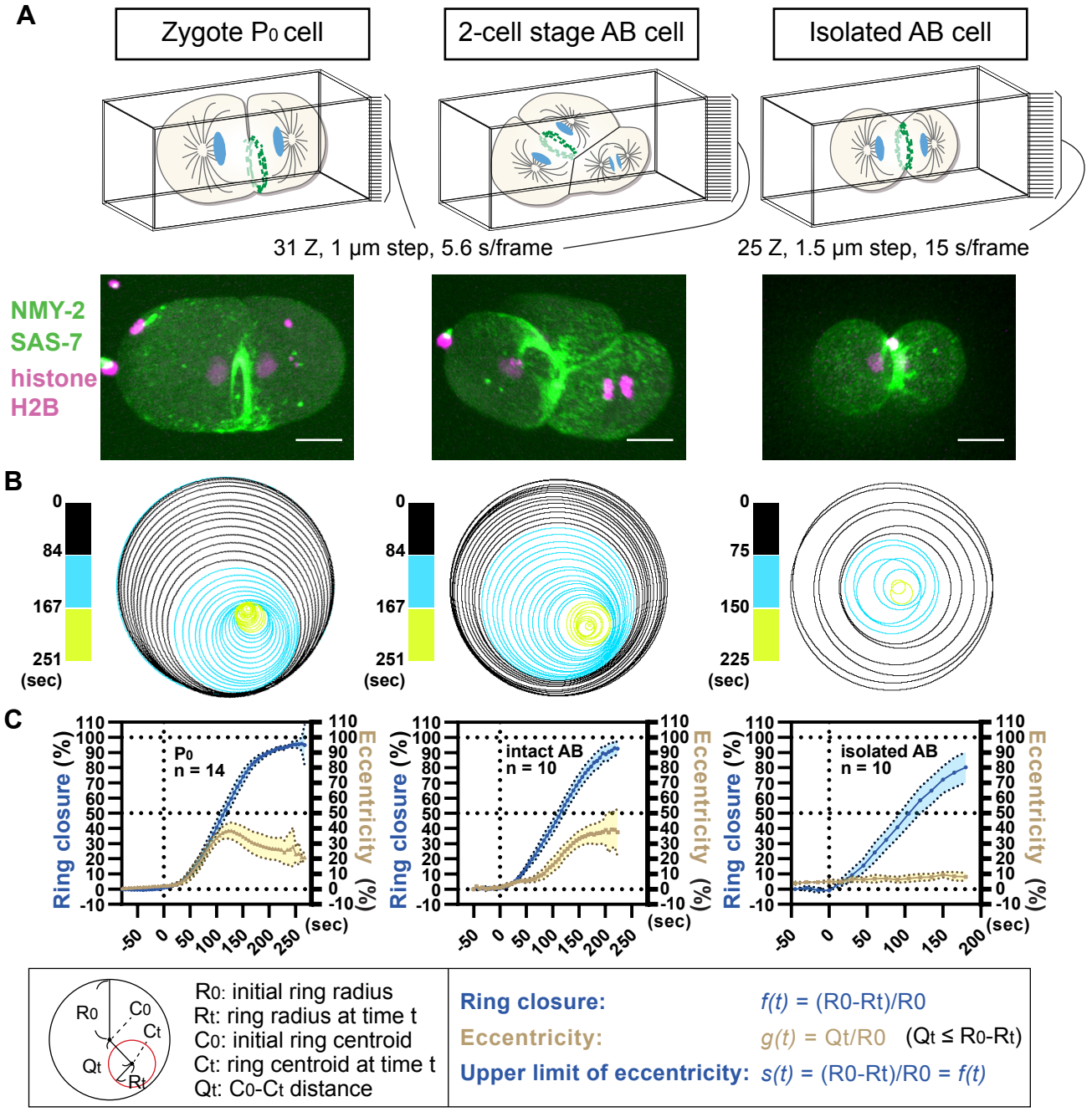

Figure 1. Intrinsic and extrinsic control of unilateral cytokinesis in *C. elegans* embryos. **(A)** Eccentric and concentric contractile ring closure of *C. elegans* embryonic blastomeres shown by volumetric 4D imaging of NMY-2::GFP (green, non-muscle myosin II), GFP::SAS-7 (green, centriole) and histone H2B::mCherry (magenta, chromosome) in the zygote P_0, 2-cell stage AB, and isolated AB. In this and subsequent figures, anterior and posterior are to the left and right, respectively. **(B)** Trajectory of ring constriction. Outlines of the contractile ring during cytokinesis are plotted for single P_0, AB, and isolated AB cells. Color coding indicates time relative to cytokinesis onset. **(C)** Mean ring closure and eccentricity. Times are relative to cytokinesis onset. Error bands indicate 95% confidence intervals. Scale bars, 10 µm.

Figure 2 (Hsu, Sangha, Fan, et al.)

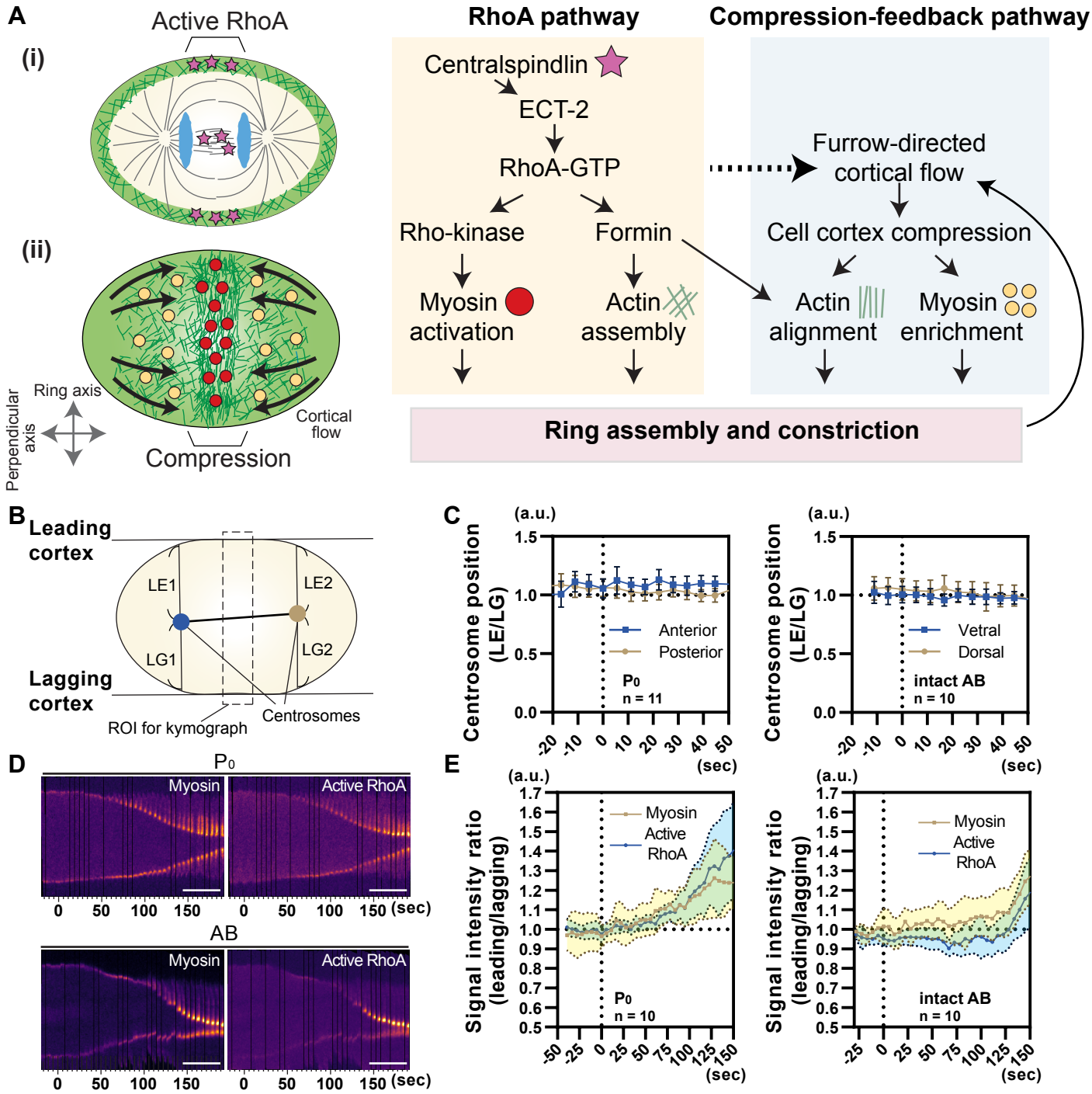

Figure 2. Mitotic spindle positioning, RhoA activity, and myosin enrichment are not asymmetric at the beginning of the P0 and AB cytokinesis.

(**A**) Contractile ring assembly mechanism in *C. elegans* zygotes. (i) Mitotic spindle positioning determines the active RhoA zone where centralspindlin activates ECT-2-RhoGEF and RhoA; RhoA-GTP then activates myosin and actin assembly ("RhoA pathway"). (ii) At the cell surface, cortical flow compresses the equatorial cell cortex, producing actin alignment and myosin enrichment. Ring constriction further pulls the cell cortex to induce pole-to-equator cortical flow to form a positive feedback loop ("compression-feedback pathway"). (**B, C**) Centrosome positions relative to the axis of contractile ring constriction. LE and LG indicate distances between the centrosome and cell cortex, respectively. (**D**) Kymographs of myosin and active RhoA localization at the equatorial cell cortex (ROI shown in B) using intensity-based color-coding. (**E**) Ratios of myosin and active RhoA signal intensities between leading and lagging cortices. Times are relative to cytokinesis onset. Error bands and bars indicate 95% confidence intervals. Scale bars, 10 μm.

Figure 3 (Hsu, Sangha, Fan, et al.)

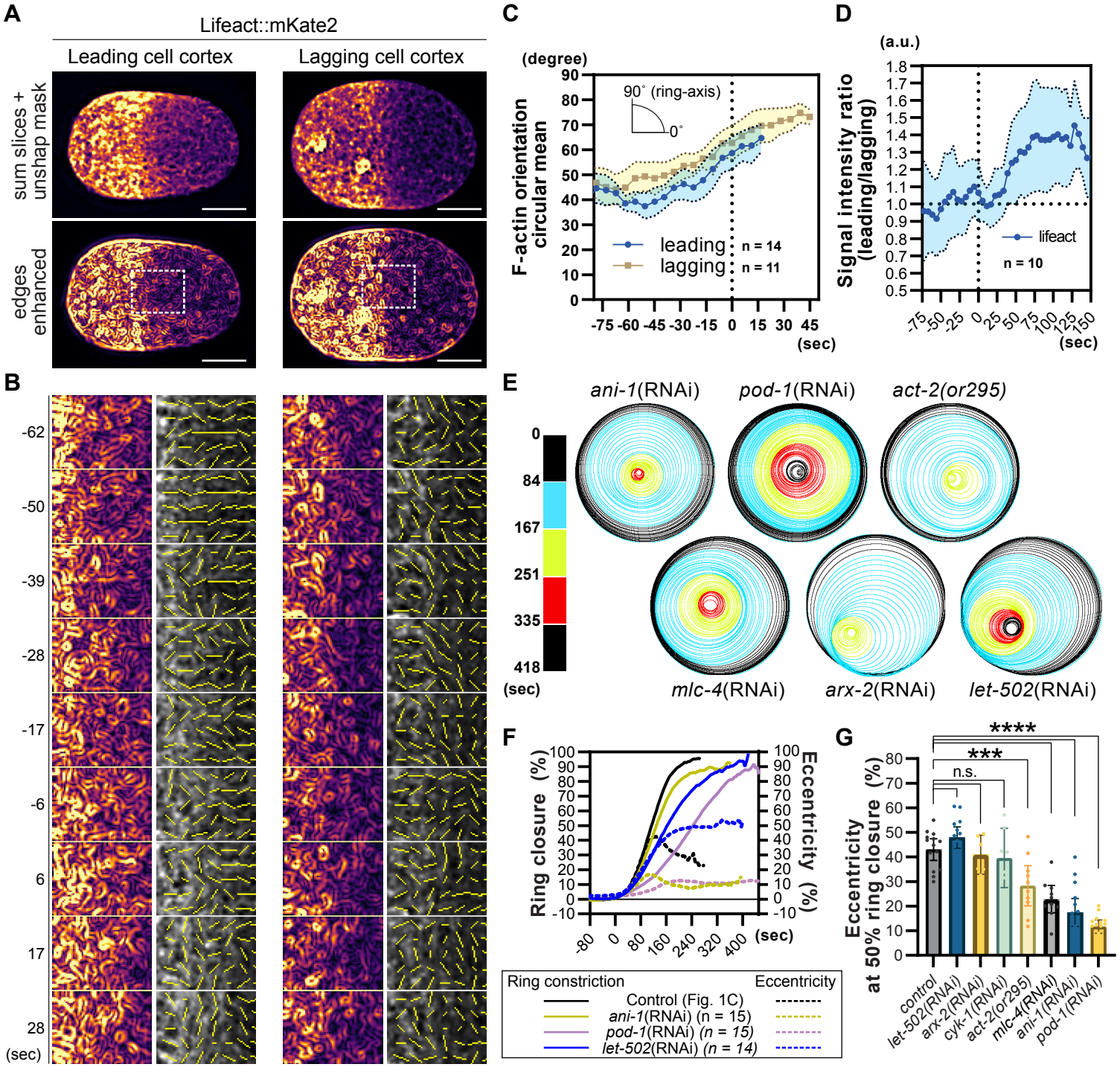

Figure 3. Actin alignment asymmetry specifies leading and lagging cell cortices of P0 cells. (**A**) F-actin distribution in leading and lagging cortices at 50 seconds before cytokinesis onset. White dotted boxes show F-actin alignments in B. Bottom panels show edge-enhanced images. (**B**) F-actin orientation at leading and lagging cell cortices. Yellow lines in the second and fourth columns indicate estimated F-actin orientations. Each box is 12 × 9 µm. (**C**) Circular means of F-actin orientation during P0 cytokinesis. (**D**) Ratios of F-actin intensities between leading and lagging cortices. (**E**) Contractile ring trajectories after perturbation of key actin and myosin regulators. (**F**) Mean ring closures and eccentricities. Control data are the same as for Fig. 1C. (**G**) Eccentricities at 50% ring closure. Times are relative to cytokinesis onset. Error bands and bars indicate 95% confidence intervals. P-values were calculated using one-way ANOVA followed by Holm-Sidak's multiple comparison test. Scale bars, 10 µm.

Figure 4 (Hsu, Sangha, Fan, et al.)

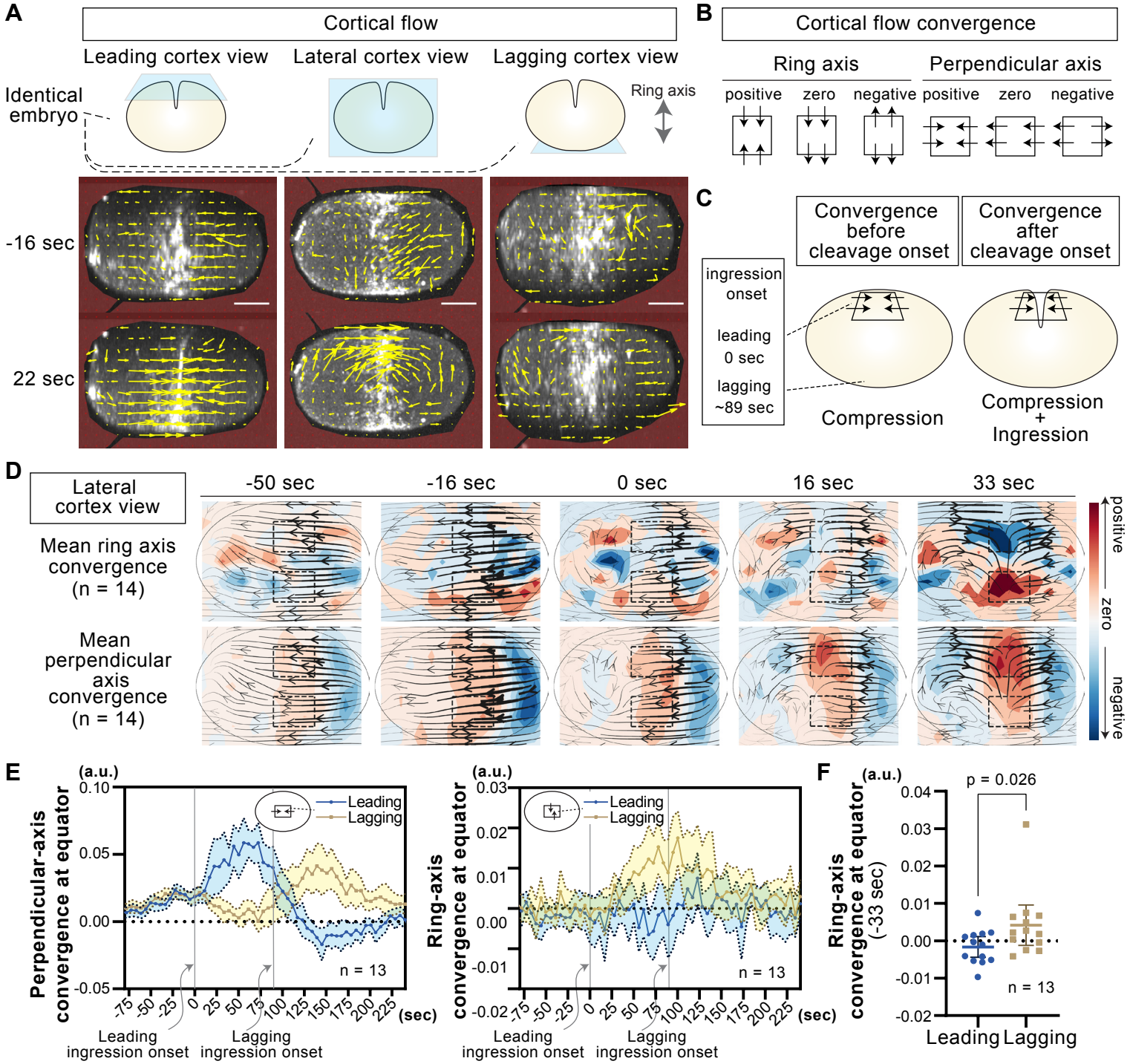

Figure 4. Lagging equatorial cortex is compressed along the contractile ring axis in P0 cells. (**A**) Cortical flow of a single embryo visualized from multiple angles. Yellow arrows indicate the movement of myosin foci from particle image velocimetry. (**B, C**) Concept of cortical convergence. Net influx and efflux of cortical flow within a certain area were calculated for the axes in parallel and perpendicular to the contractile ring (B). Cortical convergence indicates the degree of cortex compression before cleavage onset. After cleavage onset, convergence indicates both compression and the loss of cell surface from the focal plane due to invagination (C). (**D**) Mean cortical convergences and cortical flows calculated using the lateral cortex view. Arrow size scales with the cortical flow velocity. Convergence in the local area is shown by the color code. Dotted boxes indicate the equatorial regions of leading (top) and lagging (bottom) cortices. (**E**) Mean convergences at equator (boxes in schematic) calculated using leading and lagging cortex views. (**F**) Ring-axis convergences before cytokinesis onset. P-values were calculated by the Mann-Whitney U-test. Times are relative to cytokinesis onset. Error bands and bars indicate 95% confidence intervals. Scale bars, 10 μm.

Figure 5 (Hsu, Sangha, Fan, et al.)

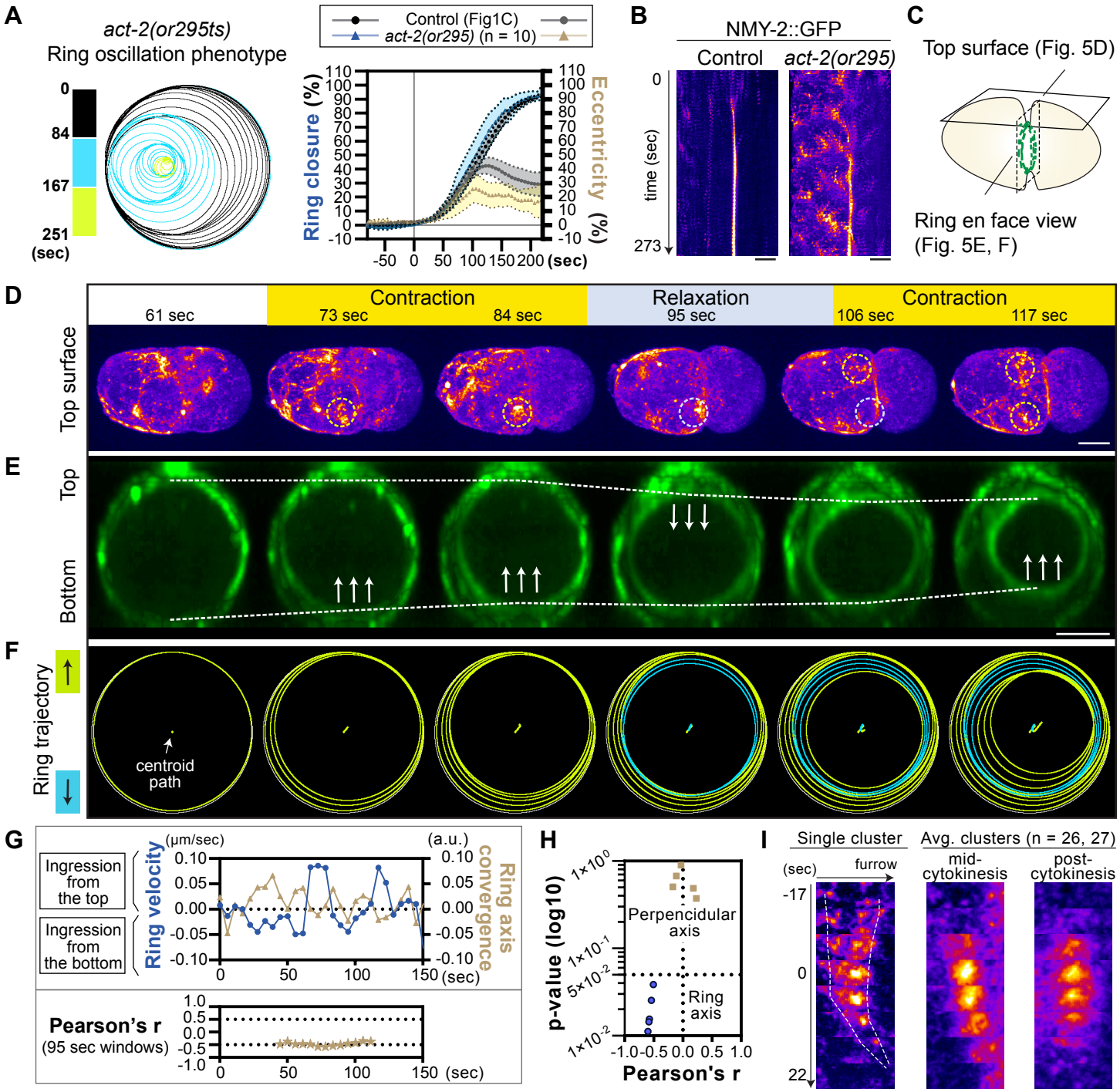

Figure 5. Ring axis compression inhibits the furrow ingression and furrow-directed cortical flow. (**A**) Contractile ring trajectory of a single *act-2(or295ts)* mutant (left panel) and the average of ten embryos (graph). (**B**) Kymographs of the cortical NMY-2::GFP with intensity-based color coding. (**C**) Planes shown in (D-F). (**D**) NMY-2::GFP localization at the top surface during cytokinesis. Yellow and light blue dotted circles indicate the area exhibiting contraction and relaxation, respectively. (**E**) Ring en face view of the same embryo shown in panel D. Dotted lines indicate top and bottom limits of the contractile ring. Arrows indicate the movement of the ring limit. (**F**) Ring trajectories of the contractile ring shown in (E). Top- and bottom-oriented movements are shown in yellow and blue, respectively. (**G**) Relationship between ring velocity and cortical convergence. Ring centroid velocities of one embryo were plotted with ring axis convergences at the top surface. Positive ring velocity represents ring ingression from the top and vice versa. Pearson's correlation coefficients in 95 sec windows are also shown. (**H**) Pearson's correlation coefficients between ring velocity and cortical convergence from five embryos. (**I**) Furrow-directed movement of myosin clusters during relaxation. Kymographs of individual and averaged clusters are shown relative to the time of peak signal intensity. Except for I, times are relative to cytokinesis onset. Error bands indicate 95% confidence intervals. Scale bars, 10 μm.

Figure 6 (Hsu, Sangha, Fan, et al.)

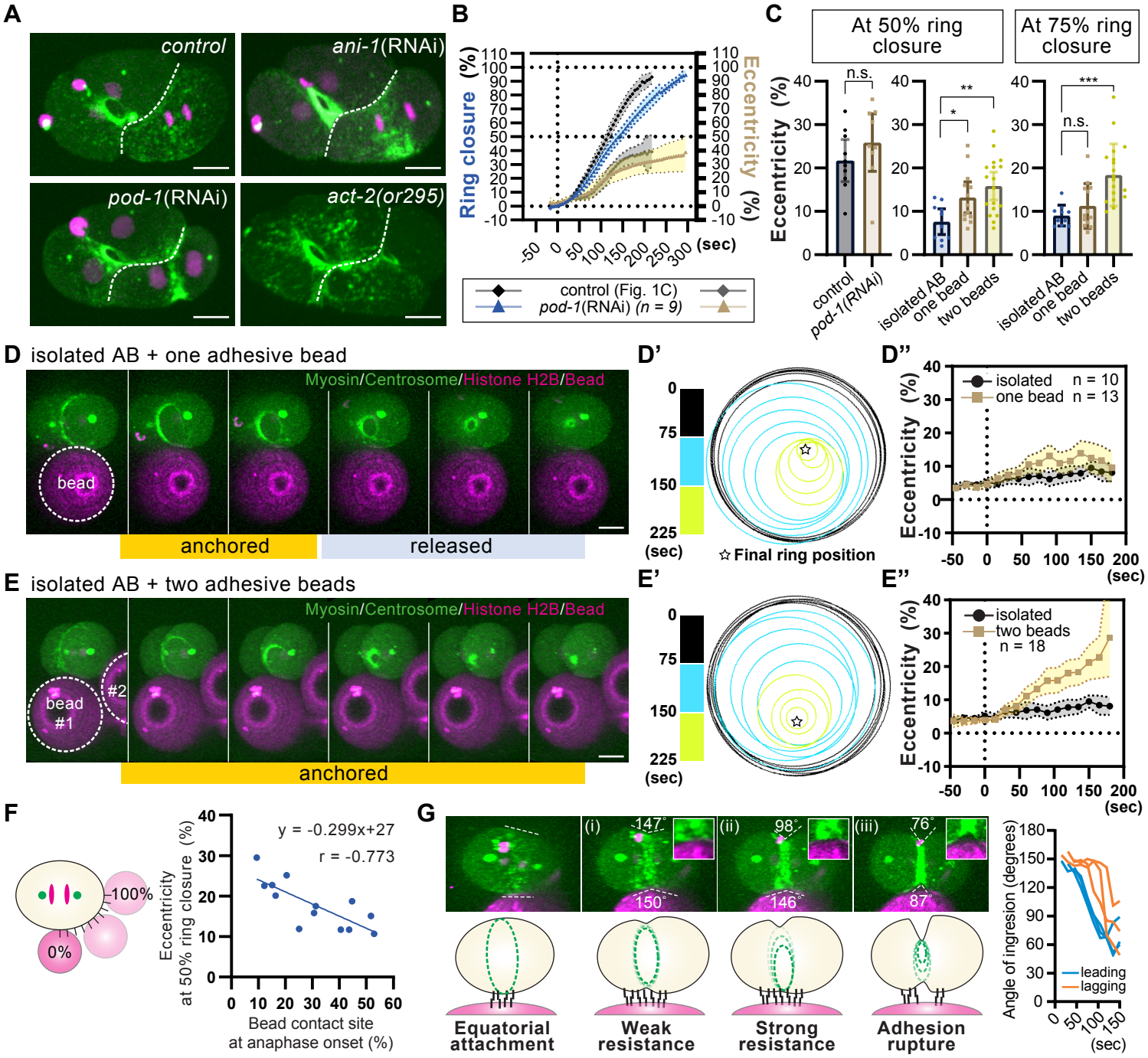

Figure 6. Adhesion results in resistance of cleavage furrow ingression in AB cells.
(**A**) Eccentric ring closure in AB cells. In addition to myosin II (green), cells are labeled with centriole (green) and histone-H2B (magenta), except for *act-2(or295ts)* mutants. White dotted lines indicate the AB-P1 boundary. (**B**) Mean ring closure and eccentricity in *pod-1*(RNAi). (**C**) Ring eccentricity in intact embryos (control vs. *pod-1*(RNAi)), and in isolated AB blastomeres with or without the attachment of adhesive beads. p-values were calculated by Welch's t-test for the left graph and one-way ANOVA with Holm-Sidak's multiple comparison test for the remaining data set. (**D, E**) Oblique view of contractile rings in the bead attached AB cell. Ring trajectory and mean eccentricity are shown in D' E' and D'' E'', respectively. (**F**) Ring eccentricity as a function of bead contact site. (**G**) Angle of ingression during adhesion-dependent unilateral cleavage. Insets in the top panels show the ring-bead interface. The graph at the right shows angles of ingression from three experiments. Times are relative to cytokinesis onset. Error bands and bars indicate 95% confidence intervals. Scale bars, 10 μm.

Figure 7 (Hsu, Sangha, Fan, et al.)

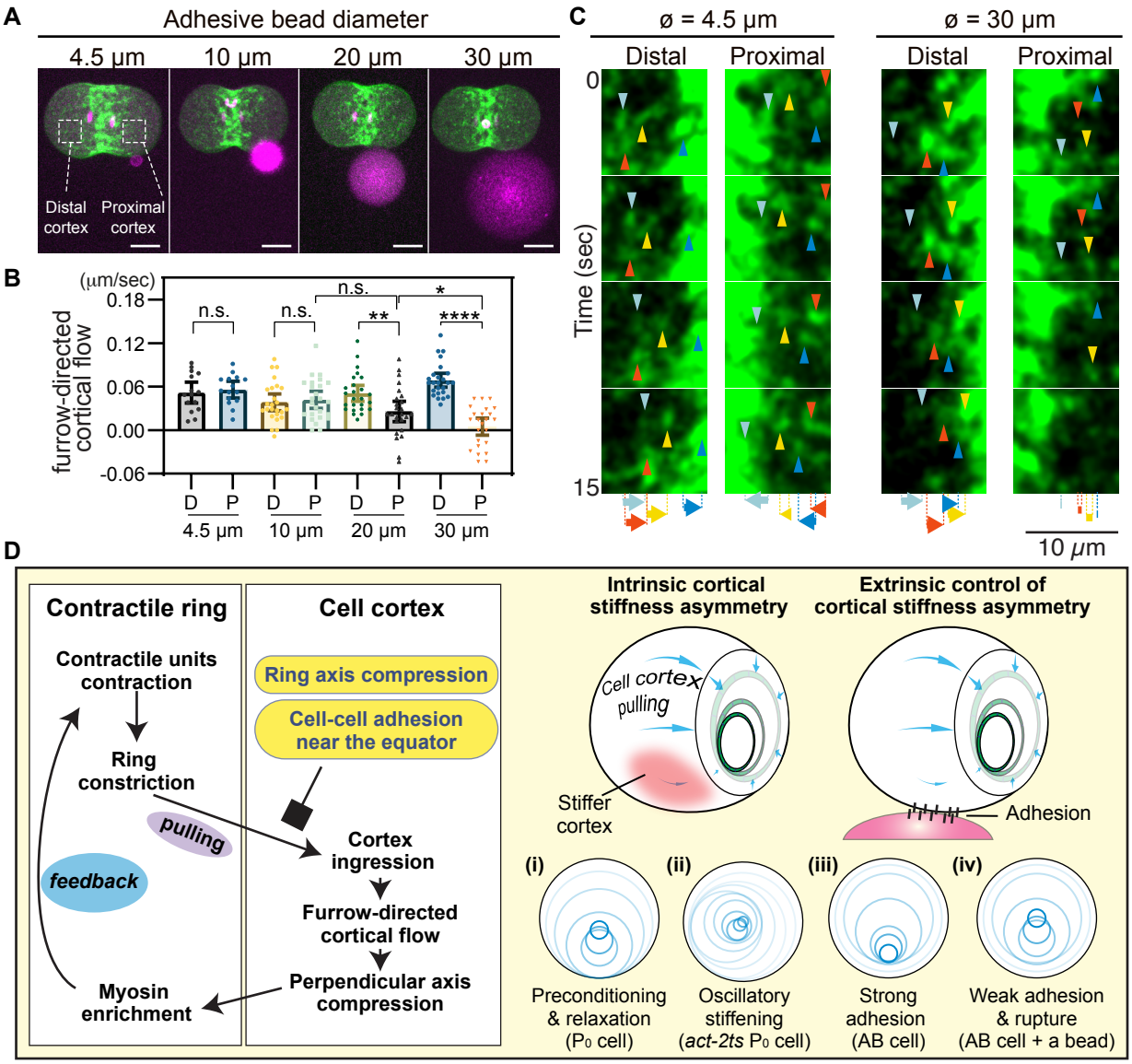

Figure 7. Adhesion inhibits furrow-directed cortical flow.
(**A**) Isolated AB cells attached to adhesive beads of different diameters. (**B**) Furrow-directed cortical flow proximal (P) and distal (D) to bead attachment sites. (**C**) Myosin movement with a bead attached. Arrowheads indicate myosin foci. Arrows below micrographs indicate total displacements over 15 sec. (**D**) Working hypothesis for symmetry-breaking in unilateral cytokinesis. Ring-axis compression and cell-cell adhesion inhibit cortical ingression and furrow-directed cortical flow by suppressing ring-dependent cortex pulling (left diagram). Perpendicular-axis compression in wild-type embryos is a result of furrow-directed cortical flow that induces myosin enrichment at the equatorial cortex through compression-dependent feedback. Suppression of cell cortex pulling induces unilateral cytokinesis with and without the compression-dependent feedback. Cortical stiffness asymmetry induced by intrinsic cortical dynamics and external adhesion is the symmetry-breaking cue (right diagram). Differences in ring trajectories can be explained by differences in the timing of stiffness change (diagrams i-iv, lower right panel). Error bars indicate 95% confidence intervals. Scale bars, 10 µm. p-values were calculated by one-way ANOVA with Holm-Sidak's multiple comparison test.

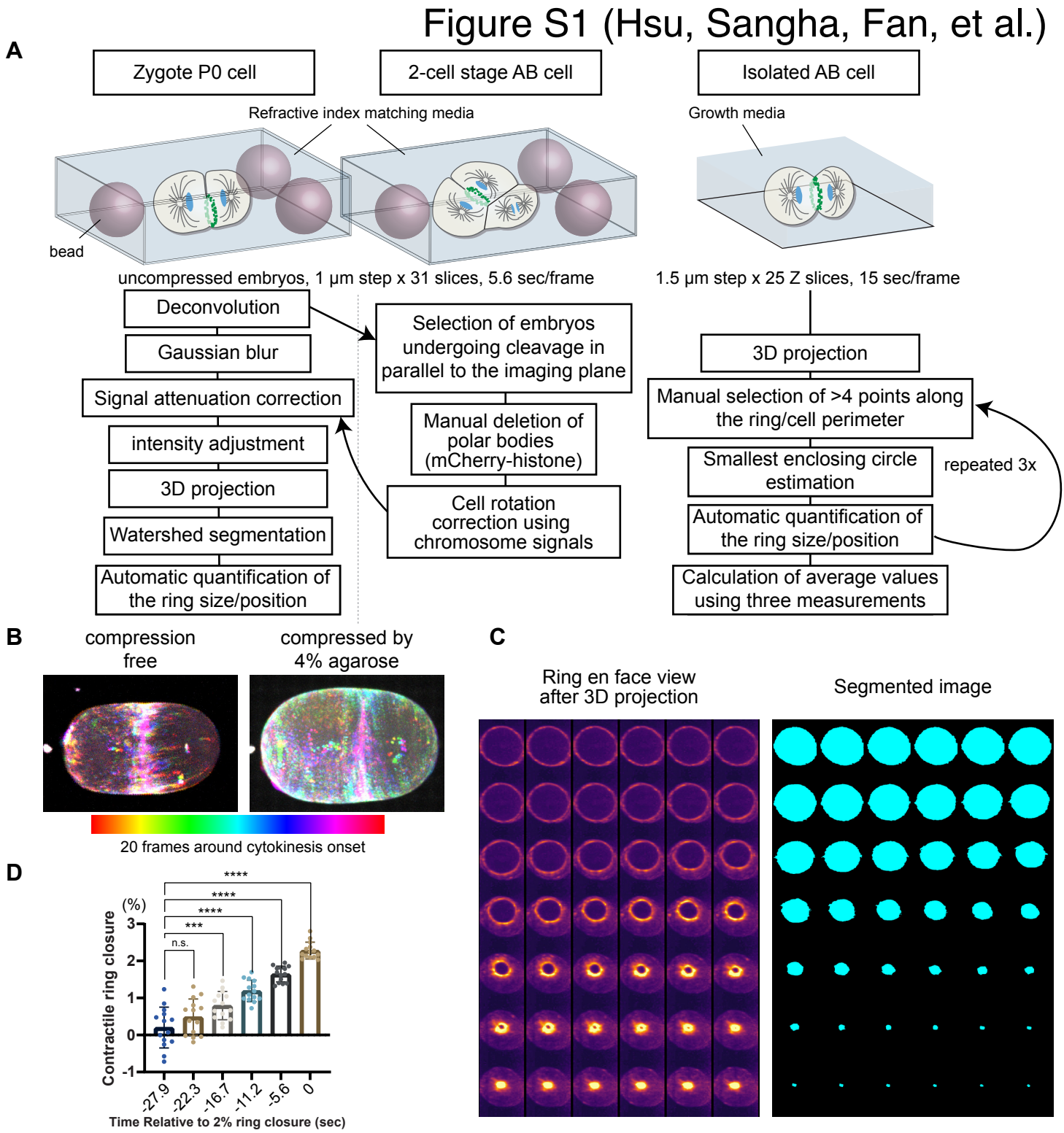

Figure S1. Imaging and contractile ring analysis methods.
(**A**) Imaging conditions and analytical flow charts. For intact embryos, we used refractive index matching medium and polystyrene beads as spacers. For isolated AB blastomeres, we used a normal growth medium and a different analytical pipeline to estimate ring size and position because of the cells' movement and rotation. Isolated AB cells were measured three times, and average values were analyzed. (**B**) Temporal color-coded image of 20 frames around cytokinesis onset showing that compression-free embryos do not exhibit global cortical rotation. (**C**) Ring en face view after the rotation of 3D projected data and ring segmentation. (**D**) Contractile ring closure data after alignment of time series data relative to 2 % ring closure. Error bars indicate 95% confidence intervals.

Figure S2 (Hsu, Sangha, Fan, et al.)

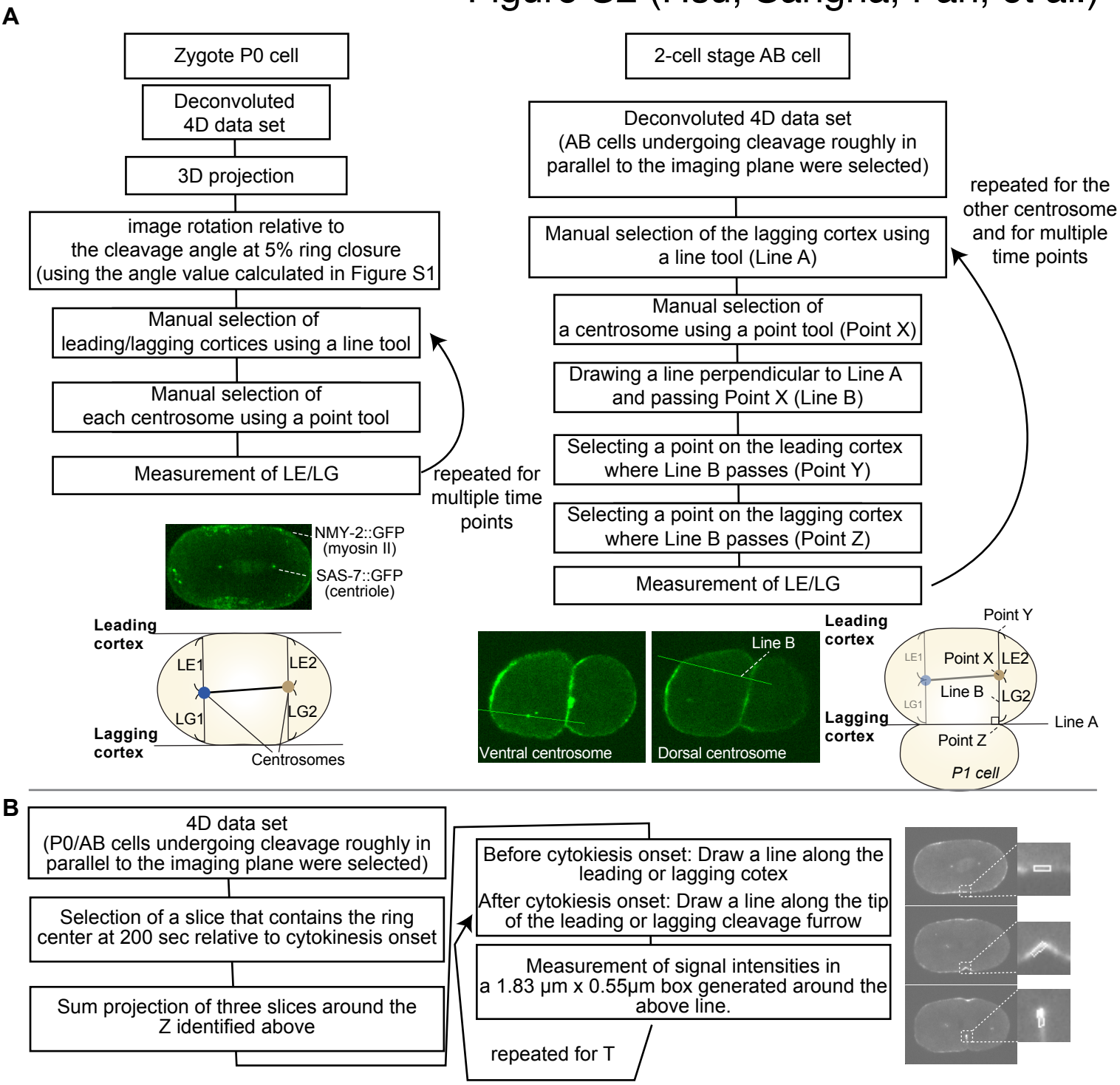

Figure S2. Measurement of centrosome positioning and signal intensity.
(**A**) Image analysis pipelines for P0 (left) and AB (right) spindle positioning. All processes were performed semi-automatically using in-house image J macros. (**B**) Image analysis pipeline for active RhoA and myosin signal intensities. White boxes in the insets of images on the right show the areas of measurement.

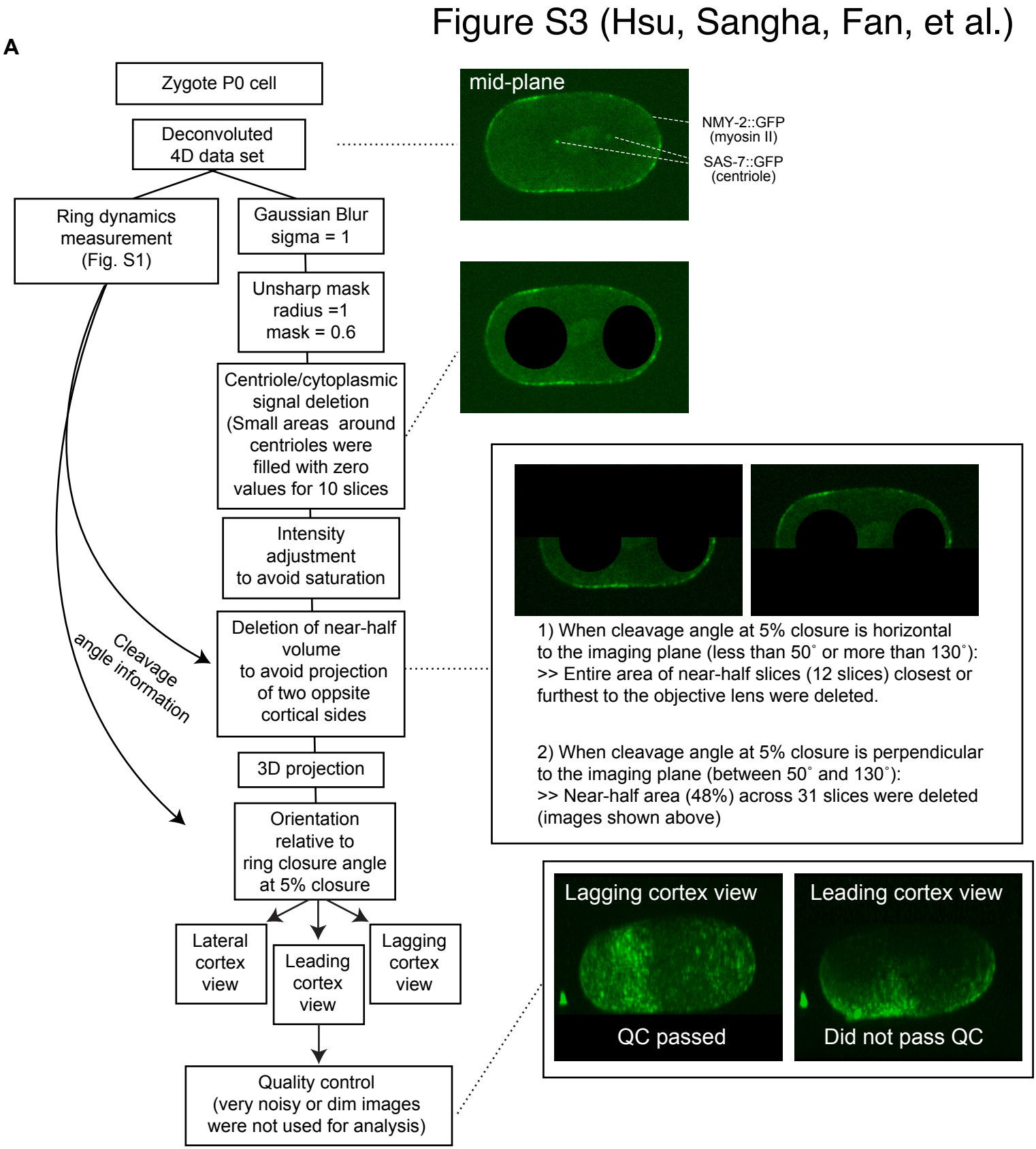

Figure S3. Generation of cortical myosin data used for PIV analysis.
(**A**) An image preprocessing pipeline used to generate cortical myosin data for Particle Image Velocimetry analyses. See also Methods section. At the quality control step, very noisy or dim images were not selected for PIV analyses. These images are usually from image planes furthest from the objective lens.